Table of contents

S1. General Experimental Remarks

Powder X-Ray Diffraction (PXRD): PXRD patterns were collected in a PANalytical X'Pert PRO diffractometer using copper radiation (Cu Kα = 1.5418 Å) with an X'Celerator detector, operating at 40 mA and 45 kV. Profiles were collected in the 3° < 2θ < 40° range with a step size of 0.017°.

Thermogravimetric Analysis (TGA): were carried out with a Mettler Toledo TGA/SDTA 851 apparatus between 25 and 800 °C under ambient conditions (10 °C·min^{-1} scan rate and an air flow of 9 mL·min−1).

Nuclear Magnetic Resonance Spectroscopy (NMR): NMR spectra were recorded on a Bruker AVIII 300 MHz spectrometer and referenced to residual solvent peaks.

Gas Uptake: N_2 adsorption isotherms were carried out at 77 K on a with a Micromeritics 3Flex gas sorption analyser. Samples were degassed under vacuum at 120 °C for 24 h in a Multisorb station prior to analysis. BET surface areas, micropore surface areas and external surface areas were calculated from the isotherms using the MicroActive operating software. The pore size distributions were calculated using Cylindrical pore oxide surface (QSDT) pore model within the MicroActive software, applying a regularisation of 10^{-2}.

Scanning Electron Microscopy (SEM) and single point energy-dispersive X-Ray analysis (EDX): particle morphologies, dimensions and mapping were studied with a Hitachi S-4800 scanning electron microscope at an accelerating voltage of 20 kV, over metalized samples with a mixture of gold and palladium during 90 seconds.

Fourier Transform Infrared Spectroscopy: IR spectra of solids were collected using a Shimadzu Fourier Transform Infrared Spectrometer, FTIR-8400S, fitted with a Diamond ATR unit.

Inductively Coupled Plasma-Mass Spectrometry: Metal content analyses were carried on an Agilent ICP-MS 7900 apparatus.

Dynamic Light Scattering: Colloidal analysis was performed by Dynamic Light Scattering (DLS) with a Zetasizer Ultra potential analyser equipped with Non-Invasive Backscatter optics (NIBS) and a 50 mW laser at 633 nm. (University of Valencia).

Density Functional Theory (DFT) Computational Calculations: All periodic DFT calculations have been performed employing Perdew–Burke–Ernzerhof (PBE)[1] functional as implemented in the Vienna ab Initio Simulation Package (VASP) [2,3] using

GW PAW potentials [4] and a 500 eV plane wave cutoff basis set. The Γ-point was used to sample the Brillouin zone and the dispersion energy corrections of the TS method [5] were computed using the Barcelona Supercomputing Center, part of the Spanish Supercomputing Network. The total DOS and the electronic band structure of the crystalline solids were calculated by using the screened hybrid functional of Heyd, Scuseria, and Ernzerhof (HSE06).[6] The electron energies were aligned to the vacuum level using a procedure reported by Butler and co-workers.[7]

Theoretical Pore Size Distribution: Pore size for each configuration was simulated using Zeo++ (chan_radious=probe_ratious=0.8 and num_samples=2000).[8]

S.2. Materials and Synthesis

All reagents unless otherwise stated were obtained from commercial sources and were used without further purification.

S.2.1. General remarks

For the synthesis of mod%-H/L series a mixture of AcOH and DMF 20:80 v:v% was used to separately dissolve the different synthetic components prior to their mixing into the reaction jars, as further explained during this section. In all syntheses the jars were placed in an oven at room temperature and heated to 120º C using 2º C/min ramp. The temperature was maintained for 48 hours and cooled down to room temperature using 0.4º C/min ramp. The resultant powder was collected by centrifugation (5000 rpm, 5 min) and washed with DMF (x2) and MeOH (x3) through dispersion-centrifugation cycles. The samples were dried under vacuum overnight and further activated by Sohxlet extraction with MeOH during approximately 24 hours. The samples were further dried under vacuum for 24 hours prior to characterization.

^{1}HNMR characterization: approximately 5 mg of the MOF were digested in 0.6 mL of DMSO-d_6 and 5 drops of D_2SO_4 by heating at 75°C and stirring until complete dissolution.

Dynamic Light Scattering (DLS) Measurements: The particle size, aggregation and colloidal dispersion were measured by dynamic light scattering (DLS) in water and dichloromethane. In a scintillation vial, dispersions of the samples with a concentration of 0.25 mgmL^{-1} were prepared by sonication over 10 minutes prior to measurement.

S.2.2. High Throughput Synthetic protocols

The synthetic conditions (**Tables S1** and **S2**) were modified from previous publications from the group:[9,10]

Procedure for the exploration of MUV-10 coordination modulation variables: $CaCl_2$ (66 mg, 1 equivalent) was dissolved in a 25 mL pyrex jar using 2 mL of the solvent mixture. In a separate vial, btc (1.5 equivalents), was dissolved in 9.8 mL of the solvent mixture. The btc solution was added to the $CaCl_2$ containing jar and the mixture was gently stirred, followed by slow Ti(IV) isopropoxide addition (1 equivalent) and gentle stirring. In the unmodulated syntheses where no AcOH is used, the same amount of final volume is reached with DMF as the only solvent. If the synthetic conditions involve the use of HCl instead of AcOH (the same volume of HCl, 2.2 mL) is added to the btc/$CaCl_2$ mixture prior to Ti(IV) isopropoxide addition. AcOH sample (solvent mixture 11.8 mL), HCl sample (9.6 mL of DMF + 2.2 mL of HCl) and unmodulated sample (11.8 mL of DMF).

Procedure for MUV-10 mod%-H series: $CaCl_2$ (66 mg, 1 equivalent) was dissolved in a 25 mL pyrex jar using 2 mL of the solvent mixture. In a separate vial, 1.5 equivalents of btc and the desired number of equivalents of modulator were dissolved in 9.8 mL of the solvent mixture. Both solutions were mixed in the pyrex jar followed by slow Ti(IV) isopropoxide addition (1 equivalent) and gentle stirring. See **Tables S1** and **S2** for tabulated values.

Procedure for MUV-10 mod%-L series: $CaCl_2$ (266 mg, 1 equivalent) was dissolved in an 80 mL pyrex jar using 10 mL of the solvent mixture. In a separate vial, 1 equivalent of

btc+mod was dissolved in 37.2 mL of the solvent mixture. The btc/mod solution was added to the $CaCl_2$ containing jar and the mixture was gently stirred, followed by slow Ti(IV) isopropoxide addition (1 equivalent) and gentle stirring. See **Tables S1** and **S2** for tabulated values.

Table S1: Tabulated synthetic conditions of iso%-H and -L.

Sample's labelling	$CaCl_2$	$Ti(O^iPr)_4$	btc	Modulator	Mod Vs btc	Mod Vs ligands
	Mass/ mmol	µL/ mmol	Mass/ mmol	Mass/ mmol	Equivalents	Mod%
MUV-10-H	66 mg 0.6 mmol	177.6 µL 0.6 mmol	189 mg 0.9 mmol	0	0	0
iso20%-H	66 mg 0.6 mmol	177.6 µL 0.6 mmol	189 mg 0.9 mmol	37.4 mg 0.225 mmol	0.25	20
iso33%-H	66 mg 0.6 mmol	177.6 µL 0.6 mmol	189 mg 0.9 mmol	74.8 mg 0.45 mmol	0.5	33
iso43%-H	66 mg 0.6 mmol	177.6 µL 0.6 mmol	189 mg 0.9 mmol	112.1 mg 0.675mmol	0.75	43
iso83%-H	66 mg 0.6 mmol	177.6 µL 0.6 mmol	189 mg 0.9 mmol	747.6 mg 4.5 mmol	5	83
iso91%-H	66 mg 0.6 mmol	177.6 µL 0.6 mmol	189 mg 0.9 mmol	1.495 g 9 mmol	10	91
iso98%-H	66 mg 0.6 mmol	177.6 µL 0.6 mmol	189 mg 0.9 mmol	7.476 g 45 mmol	50	98
iso25%-L	266 mg 2.4 mmol	710 µL 2.4 mmol	307 mg 1.8 mmol	100 mg 0.60 mmol	0.33	25
iso50%-L	266 mg 2.4 mmol	710 µL 2.4 mmol	295 mg 1.2 mmol	199 mg 1.20 mmol	1	50
iso60%-L	266 mg 2.4 mmol	710 µL 2.4 mmol	240 mg 0.96mmol	239 mg 1.44 mmol	1.5	60
iso70%-L	266 mg 2.4 mmol	710 µL 2.4 mmol	122 mg 0.72 mmol	279 mg 1.68 mmol	2.33	70
iso80%-L	266 mg 2.4 mmol	710 µL 2.4 mmol	319 mg 0.48mmol	318 mg 1.92 mmol	4	80
iso90%-L	266 mg 2.4 mmol	710 µL 2.4 mmol	40.96 mg 0.24 mmol	358 mg 2.16 mmol	9	90

*Note that MUV-10-H refers to MUV-10 AcOH-H.

Table S2: Tabulated synthetic conditions of benzo%- H and L.

Sample's labelling	$CaCl_2$	Ti(OiPr)4	btc	Modulator	Mod Vs btc	Mod Vs ligands
	Mass/ mmol	µL/ mmol	Mass/ mmol	Mass/ mmol	Equivalents	Mod%
MUV-10-H	66 mg 0.6 mmol	177.6 µL 0.6 mmol	189 mg 0.9 mmol	0	0	0
benzo33%-H	66 mg 0.6 mmol	177.6 µL 0.6 mmol	189 mg 0.9 mmol	55mg 0.45 mmol	0.5	33
benzo50%-H	66 mg 0.6 mmol	177.6 µL 0.6 mmol	189 mg 0.9 mmol	110 mg 0.9 mmol	1	50
benzo67%-H	66 mg 0.6 mmol	177.6 µL 0.6 mmol	189 mg 0.9 mmol	220 mg 1.8 mmol	2	67
benzo83%-H	66 mg 0.6 mmol	177.6 µL 0.6 mmol	189 mg 0.9 mmol	550 mg 4.5 mmol	5	83
benzo91%-H	66 mg 0.6 mmol	177.6 µL 0.6 mmol	189 mg 0.9 mmol	1.099 g 9 mmol	10	91
benzo98%-H	66 mg 0.6 mmol	177.6 µL 0.6 mmol	189 mg 0.9 mmol	5.595 g 45 mmol	50	98
benzo50%-L	266 mg 2.4 mmol	710 µL 2.4 mmol	295 mg 1.2 mmol	176 mg 1.20 mmol	1	50
benzo70%-L	266 mg 2.4 mmol	710 µL 2.4 mmol	122 mg 0.72 mmol	205 mg 1.68 mmol	2.33	70
benzo80%-L	266 mg 2.4 mmol	710 µL 2.4 mmol	102 mg 0.48mmol	235 mg 1.92 mmol	4	80
benzo90%-L	266 mg 2.4 mmol	710 µL 2.4 mmol	40.96 mg 0.24 mmol	264 mg 2.16 mmol	9	90

*Note that MUV-10-H refers to MUV-10 AcOH-H.

S.3. Optimization of the synthesis of defect-free MUV-10 phases

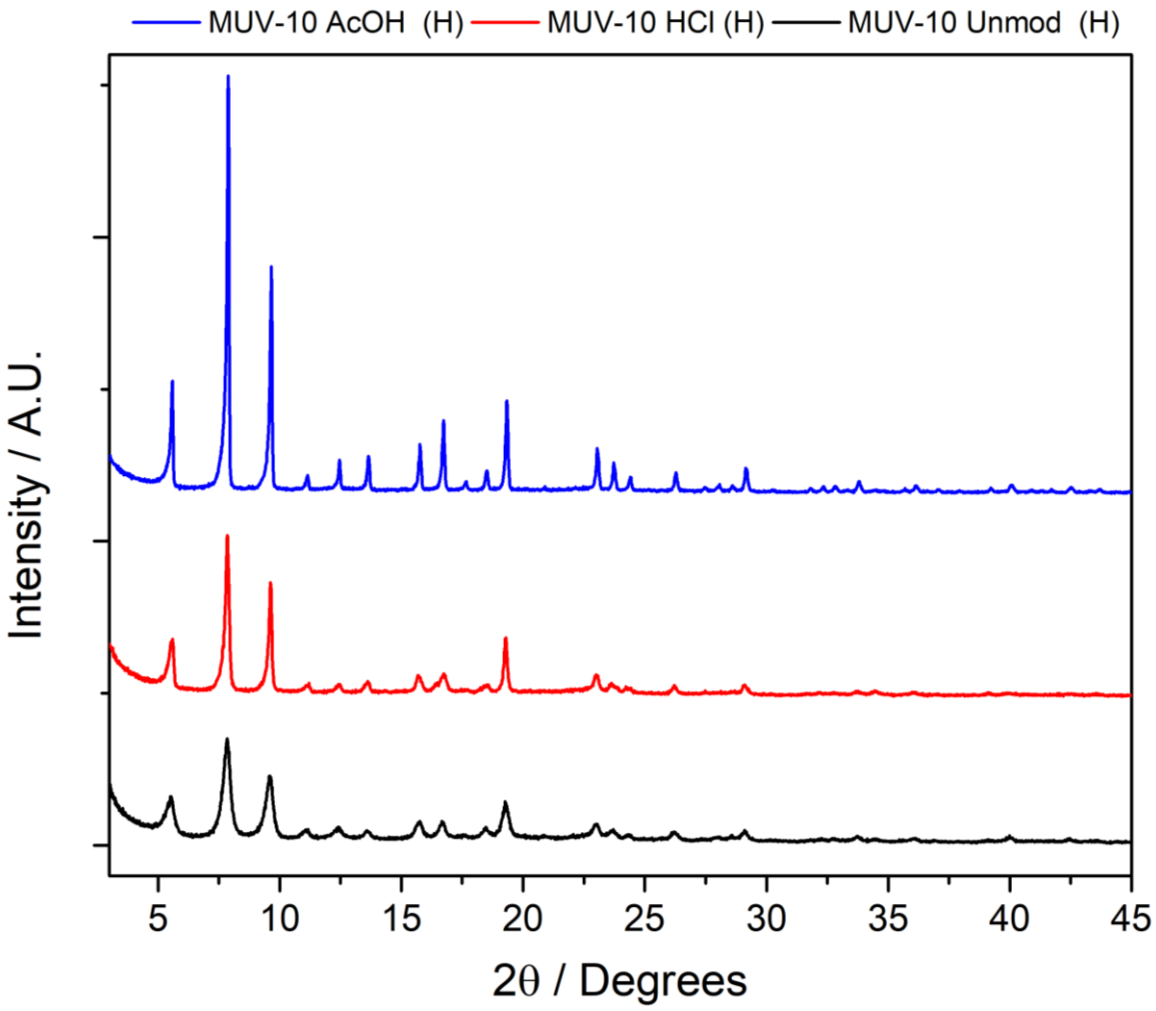

Figure S1: PXRD patterns of MUV-10 synthesized in the presence of AcOH, HCl or unmodulated conditions.

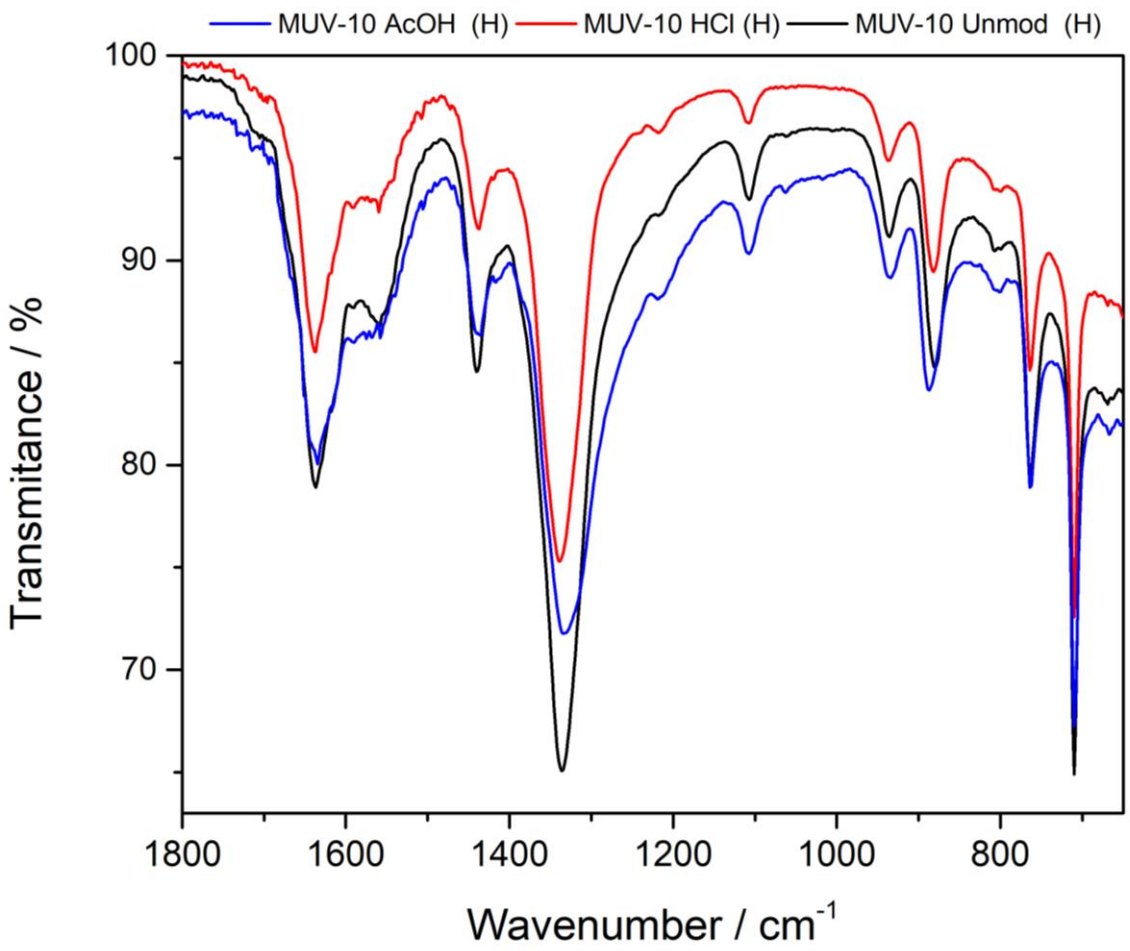

Figure S2: FT-IR of MUV-10 synthesized in the presence of AcOH, HCl or unmodulated conditions, showing negligible changes in the vibration bands.

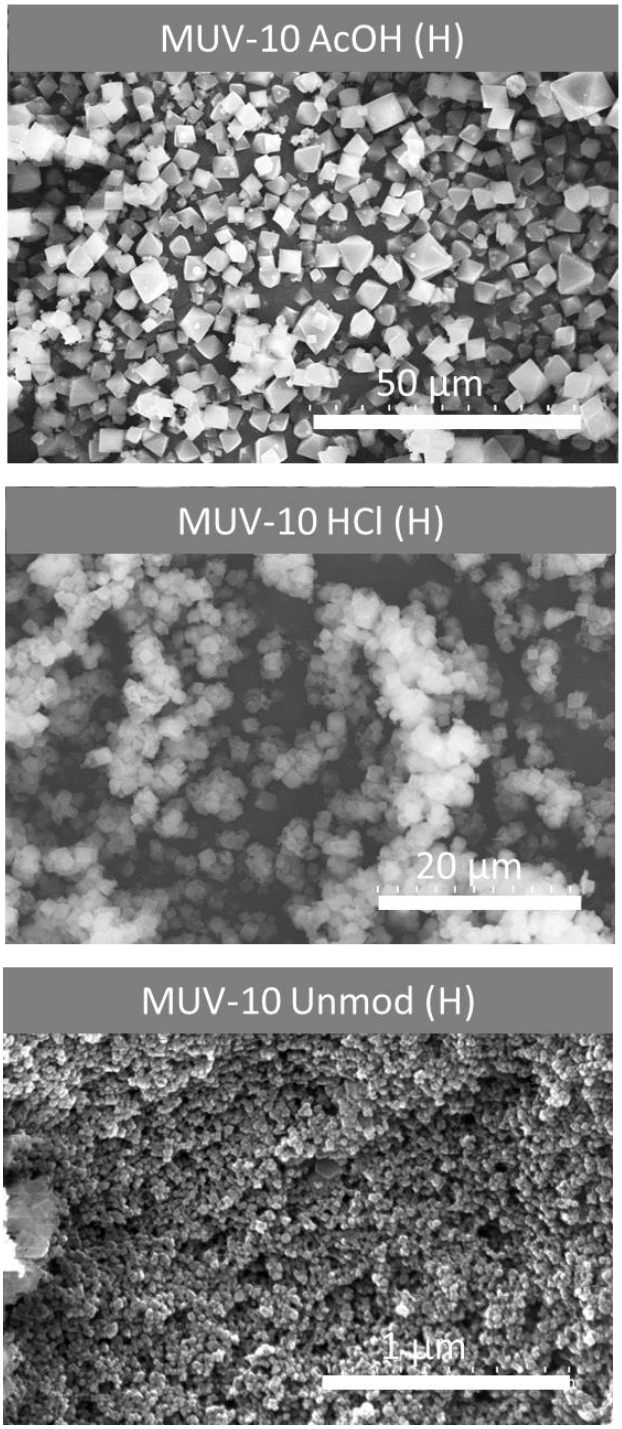

Figure S3: SEM images of MUV-10 synthesized in the presence of AcOH, HCl or unmodulated conditions.

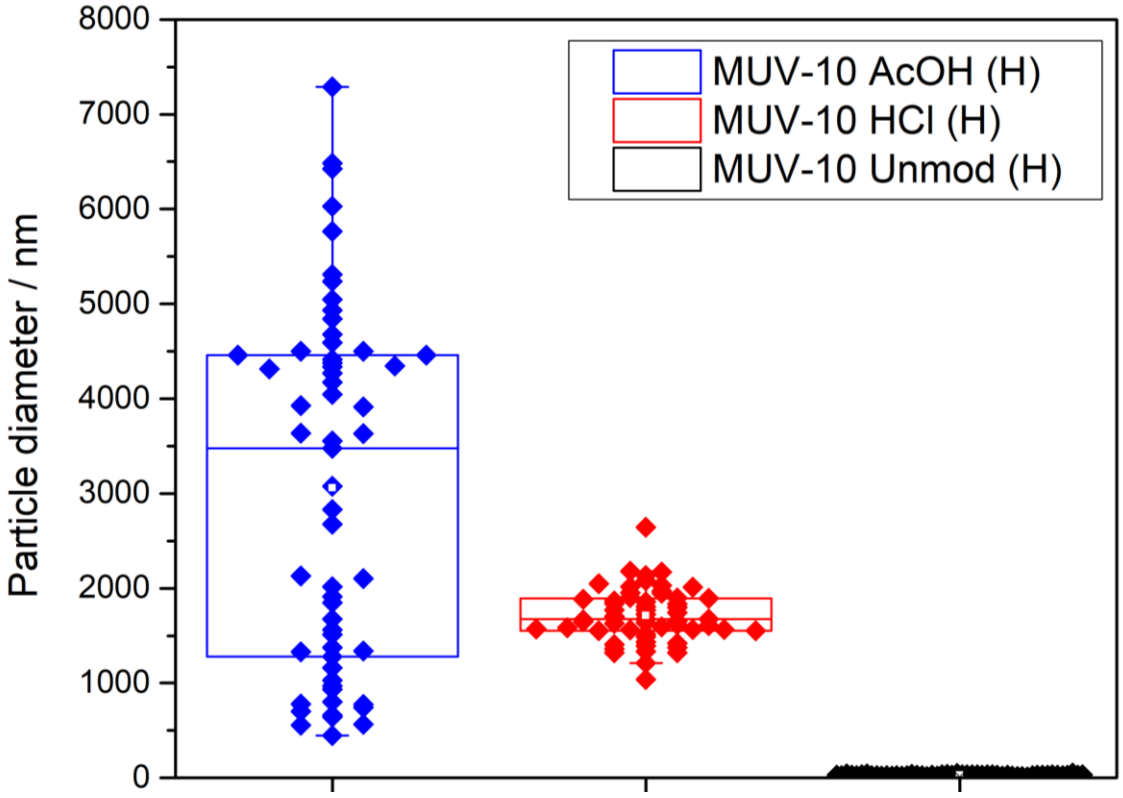

Figure S4: Statistic box charts displaying particle size of MUV-10 synthesized under different conditions. The box chart represents the average ± standard deviation particle size, alongside with the 25% and 75% percentiles for a bin size of 50 nm and particle size count higher than 50. Compared to AcOH, HCl addition results in a more homogeneous distribution of particle sizes with no statistical difference in size. The particle size of the unmodulated MOF drastically decreases, suggesting faster nucleation. These results suggest that AcOH acts as a pH regulator and a crystal growth promoter modulator.

Table S3: Tabulated particle sizes, standard deviations, and metal content in mole per cent versus the total metal content (determined by EDX) of MUV-10 in presence of AcOH, HCl or unmodulated conditions. For a pristine structure, the theoretical Ca:Ti ratio is 1:1.

Sample	Particle size (SD) (nm)	% Ca	% Ti
MUV-10 AcOH	3064 (1933)	46.7	53.3
MUV-10 HCl	1710 (280)	48.18	51.82
MUV-10 unmod	28.1 (7.7)	46.73	53.27

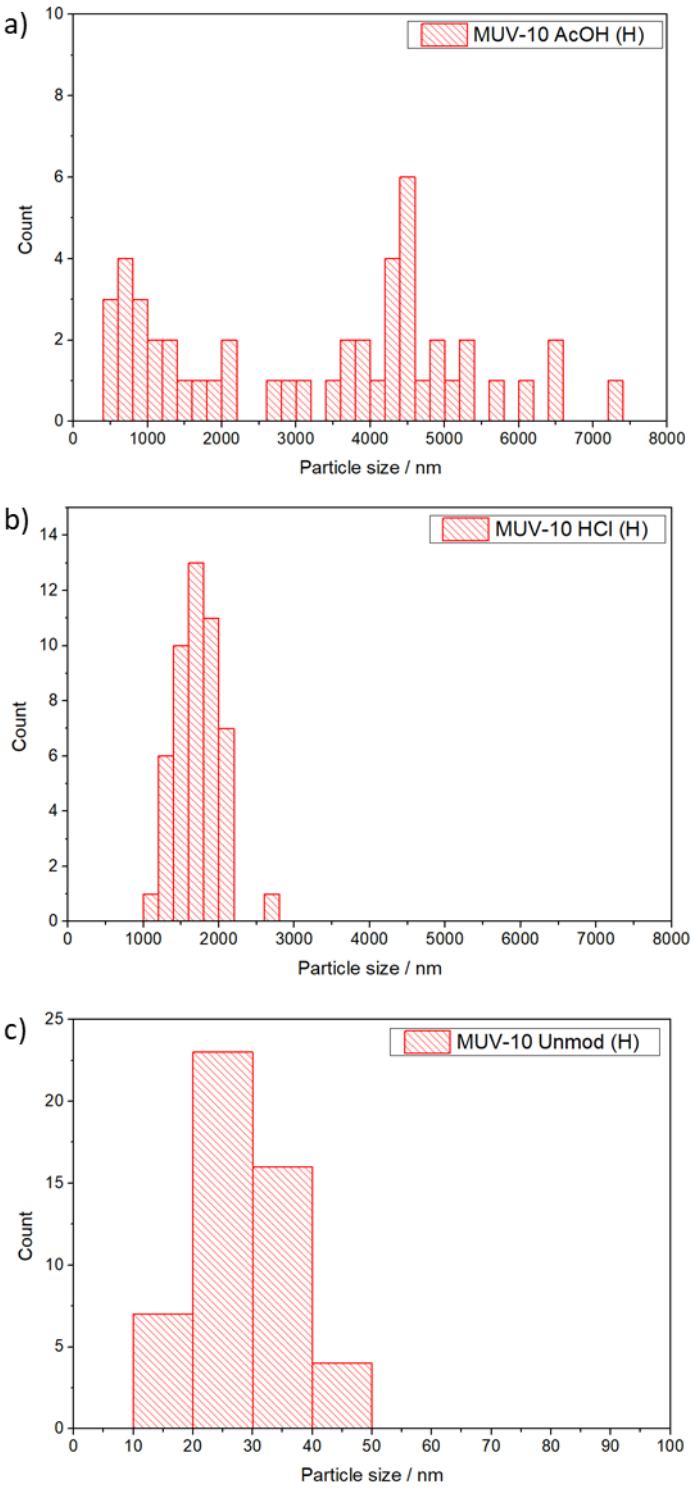

Figure S5: Histograms of the particle size distribution of MUV-10 synthesised under different conditions for a particle count of 50. Bin size of 200 nm for upon AcOH and HCl modulation and 10 nm for the unmodulated synthesis.

Table S4: Tabulated data extracted from ^{1}HNMR of acid digested MUV-10 samples synthesized in the presence of AcOH, HCl or unmodulated conditions. formic acid (fa) in the structure is expressed as **mole ratio** (i.e. $\text{fa ratio} = \frac{\text{fa}}{\text{btc}}$) and **mole per cent** (i.e. fa mol% $= \frac{\text{fa}}{\text{fa} + \text{btc}} * 100$).

Sample	fa mol%	fa ratio
MUV-10 AcOH	1	0.010
MUV-10 HCl	1.5	0.015
MUV-10 Unmod	3.7	0.038

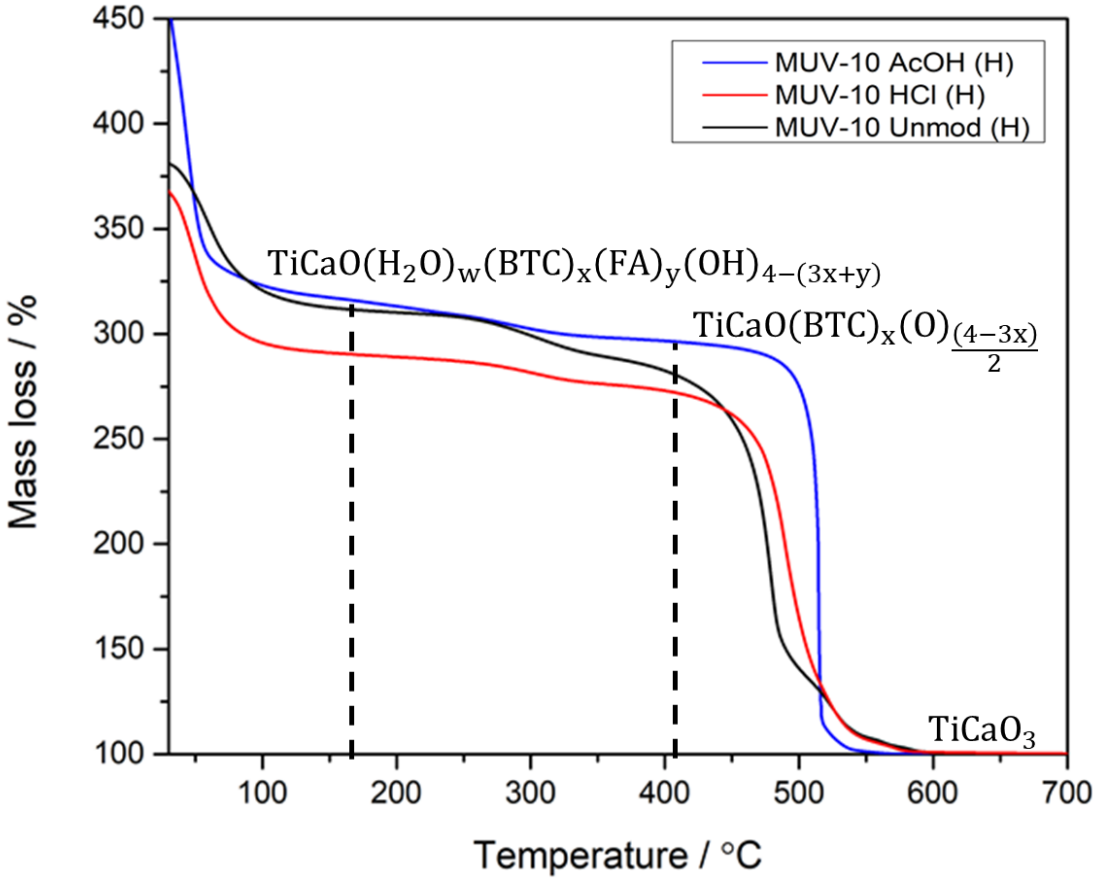

Figure S6: TGA profiles of MUV-10 samples synthesised under different conditions. The proposed formulas after the desorption of pore solvent/water (T=160 ºC) and dehydration and decomposition modulator molecules (T=410 °C) have been added for clarity. Data has been normalized to the mass of the $TiCaO_3$ residue.

Inspired by Lilleroud *et. al.,*[11,12] to provide a direct comparison of the mass loss of different materials we have normalized the residues to 100% **(Figure S6)**. We have performed our calculations based on the experimental mass ratio between the structure and its residue using methodology recently reported by one of us.[13]

For MUV-10 DH the molecular formula should be $TiCaO(btc)_X(O)_{(4-3X)/2}$, where oxygens coming from defect compensating species previously decomposed compensate for the missing linker's charge,[12,13] and the metal residue should be $TiCaO_3$. Then, the ratio between the MOF and the residue should be as follows:

$$\text{Experimental}\frac{\text{DH MOF}}{\text{Residue}}\text{Ratio}\left(R_{expDH}\right)=\frac{M_w\,[T410\,°C]}{M_w[\text{Residue}]}=\frac{M_w\,[TiCaO(btc)_x(O)_{\left(\frac{(4-3x)}{2}\right)}]}{M_w\,[TiCaO_3]}$$

Hence,

$$X\,btc=\frac{\left(R_{expDH}*\ M_w\,[TiCaO_3]\right)-\text{Mass TiCaO}-2*M_w[O]}{M_w\,[btc]-\left(\frac{3}{2}\right)*M_w[O]}$$

$$\text{Number of Formate}=\text{number of btc}*\left(\frac{fa}{btc}\right)\text{NMR ratio}$$

Since Cl^- species were not observed by EDX, we have assumed that OH^- ligands are compensating for the overall charge balance. Hence, the number of OH^- needed to compensate the charge can be calculated using the charge balance equation:

$$4Ti+2Ca=2+3xbtc+xNMRfa+zOH$$

Then $zOH\ =4-3xbtc-xNMRfa$

Once the number of linkers, modulators and defect-compensating species has been determined, number of water molecules is calculated as:

$$\text{Experimental}\frac{\text{MOF}}{\text{Residue}}\text{Ratio}\left(R_{exp}\right)=\frac{M_w\,[T\ 160\,°C]}{M_w[\text{Residue}]}=\frac{M_w\,[TiCaO(btc)_x(H_2O)_w(Mod)_y(OH)_z]}{M_w\,[TiCaO_2]}$$

$$\text{Experimental}\frac{\text{MOF}}{\text{Residue}}\text{Ratio}\left(R_{exp}\right)=\frac{M_w\,[\text{Calculated MOF}]+w*M_w\,[H_2O]}{M_w\,[TiCaO_3]}$$

$$w\,(H_2O)=\frac{\left(R_{exp}*\ M_w\,[TiCaO_3]\right)-M_w\,[\text{Calculated MOF}]}{M_w\,[H_2O]}$$

The calculated structure **(Table S5)** is then used to calculate its mass per cent before decomposition and these values are compared with the experimental values to validate the method **(Table S6)**, alongside with the calculated coordination positions, which for a pristine $TiCaO(H_2O)_2(btc)_{1.33}$ should be 13 (7-coordinated Calcium and 6-coordinated Titanium). [9]

Table S5: Molecular formula of MUV-10 samples synthesised in the presence of AcOH, HCl or unmodulated conditions as extracted from TGA.

Sample	R_{expDH}	NMR fa/btc	Calculated structure	ML%
MUV-10	289	0.010	$TiCaO(H_2O)_2(btc)_{1.40}(fa)_{0.01}$	-0.7%
MUV-10 HCl	271	0.015	$TiCaO(H_2O)_{1.1}(btc)_{1.27}(fa)_{0.02}(OH)_{0.17}$	6.4%
MUV-10 unmod	266	0.038	$TiCaO(H_2O)_{2.8}(btc)_{1.23}(fa)_{0.04}(OH)_{0.26}$	10.1%

Table S6: Experimental mass per cent at t 160℃ in comparison with the calculated mass % based on the calculated structures **(Table S5)** both with and without axial water molecules, alongside with coordinating positions.

Sample	R_{exp}	R_{theo}	R_{expDH}	R_{theoDH}	Coordination positions (CP)
MUV-10	312	312	289	289	13.26
MUV-10 HCl	290	290	271	271	11.96
MUV-10 unmod	309	309	266	266	13.51

Table S7: Tabulated porosimetry extracted from N_2 adsorption and desorption measurements of MUV-10 samples synthesized under different conditions, showing that microporosity is higher upon AcOH addition.

Sample	S_{BET} / S_{MICRO} (m^2/g)	Micro / Meso pores volume (cm^3/g)		Total Pore volume (cm^3/g)
MUV-10 AcOH	1041 / 975	0.365	0.008	0.373
MUV-10 HCl	935 / 853	0.326	0.071	0.397
MUV-10 unmod	745 / 552	0.221	0.489	0.710

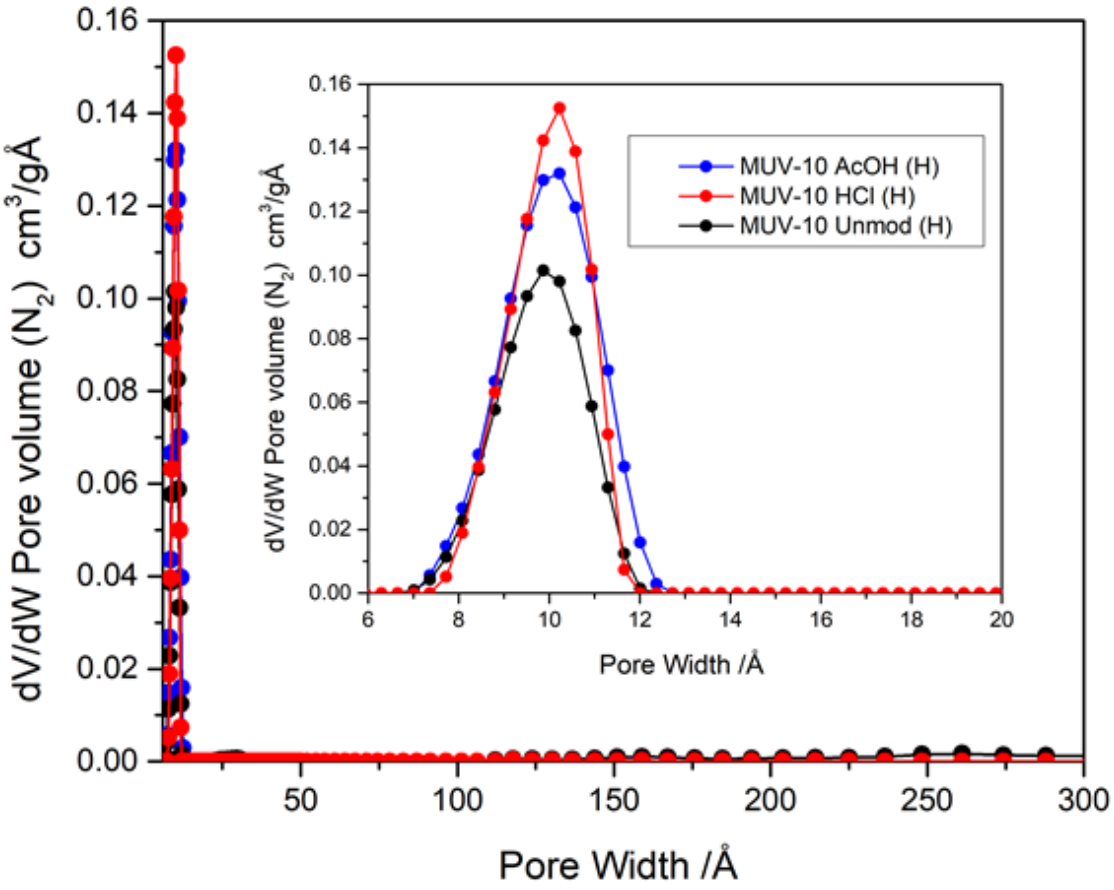

Figure S7: Pore size distributions of MUV-10 samples synthesized under different experimental conditions. Data was obtained from N_2 adsorption/desorption isotherms using a Cylindrical pore oxide surface model (QSDT).

S.4. Scope of synthetic conditions used to explore defect engineering of MUV-10.

Table S8: Table enclosing btc/metal ratio (equivalents), percentage of btc present in the synthesis in comparison to the pristine unit formula (1.33 eq.), the number of equivalents of modulator compared to metal and to linker, and the percentage of modulator versus the total amount of ligands (linker + modulator).

Sample's labelling mod= iso or benzo	btc vs metal	btc vs pristine	mod vs metal	mod vs btc	mod vs total ligands
	Eqs	%	Eqs	Eqs	%
MUV-10-H	1.5	112.78	0	0	0
mod20%-H	1.5	112.78	0.375	0.25	20.00
mod33%-H	1.5	112.78	0.75	0.50	33.33
mod43%-H	1.5	112.78	1.11	0.75	42.58
mod50%-H	1.5	112.78	1.5	1.00	50.00
mod67%-H	1.5	112.78	3	2.00	66.67
mod83%-H	1.5	112.78	7.5	5.00	83.33
mod91%-H	1.5	112.78	15	10.00	90.91
mod98%-H	1.5	112.78	75	50.00	98.04
MUV-10-L	1	75.19	0	0	0.00
mod25%-L	0.75	56.39	0.25	0.33	25.00
mod50%-L	0.5	37.59	0.5	1.00	50.00
mod60%-L	0.4	30.08	0.6	1.50	60.00
mod70%-L	0.3	22.56	0.7	2.33	70.00
mod80%-L	0.2	15.04	0.8	4.00	80.00
mod90%-L	0.1	7.52	0.9	9.00	90.00

*Note that MUV-10-H refers to MUV-10 AcOH-H.

S.5. Defect incorporation in conditions adequate for MUV-10 formation: characterization of MUV-10 mod%-H.

S.5.1 Incorporation of modulators in MUV-10 iso%-H and benzo%-H as estimated with ^{1}H-NMR.

Both isophthalic acid and benzoic acid modulator were present in the ^{1}H-NMR profiles alongside with formic acid coming from the decomposition of DMF during the synthesis. Incorporation of modulator and formic acid is expressed as the **molar ratio** (ratio) between modulator and btc, $\text{Ratio} = \frac{\text{Mod}}{\text{btc}}$ and as the **mole per cent** of modulator (mol%) compared to btc, $\text{mol\%} = \frac{\text{Mod}}{\text{Mod+btc}} * 100$.

Table S9: Tabulated ^{1}H-NMR data from acid digested iso%-H samples. Data shows iso and formic acid content increasing with the addition of modulator up to iso98%-H that does not have formic acid incorporated into the structure.

Sample	iso mol %	fa mol %	iso ratio	fa ratio
iso20%-H	1.31	1.09	0.013	0.011
iso33%-H	2.34	1.91	0.024	0.019
iso43%-H	3.49	0.93	0.036	0.009
iso83%-H	18.88	5.08	0.233	0.054
iso91%-H	28.93	9.24	0.407	0.102
iso98%-H	45.32	0	0.829	0.000

Table S10: Tabulated ^{1}H-NMR data from acid digested benzo%-H. Data shows benzo and formic acid content increasing with the addition of modulator, although to a lesser extent than upon the addition of isophthalic acid.

Sample	benzo mol %	fa mol %	benzo ratio	fa ratio
benzo33%-H	0.151	2.113	0.002	0.022
benzo50%-H	0.327	0.984	0.003	0.010
benzo67%-H	0.862	6.757	0.009	0.072
benzo83%-H	2.530	2.555	0.026	0.026
benzo91%-H	4.365	2.536	0.046	0.026
benzo98%-H	5.079	4.679	0.054	0.049

S.5.2 FT-IR of MUV-10 mod%-H.

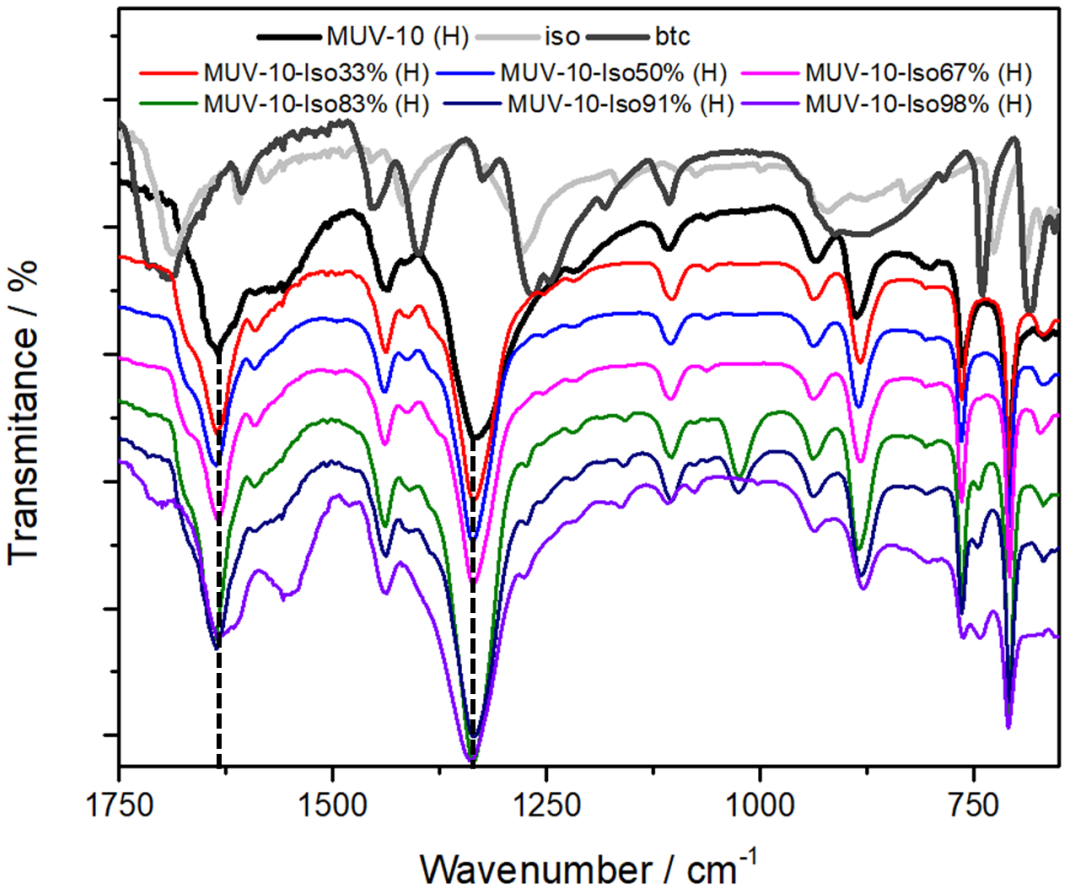

Figure S8*:* Comparison of FT-IR profiles of MUV-10 H, iso, btc, iso 100% and iso%-H. iso%-H series show characteristic vibration bands (ca. 1700 cm^{-1}) from the modulator but no free carboxylate vibrations apart from iso98% confirming modulator´s attachment to the metal clusters. No shifting in the two major MUV-10 vibration bands (dashed) are observed in any case.

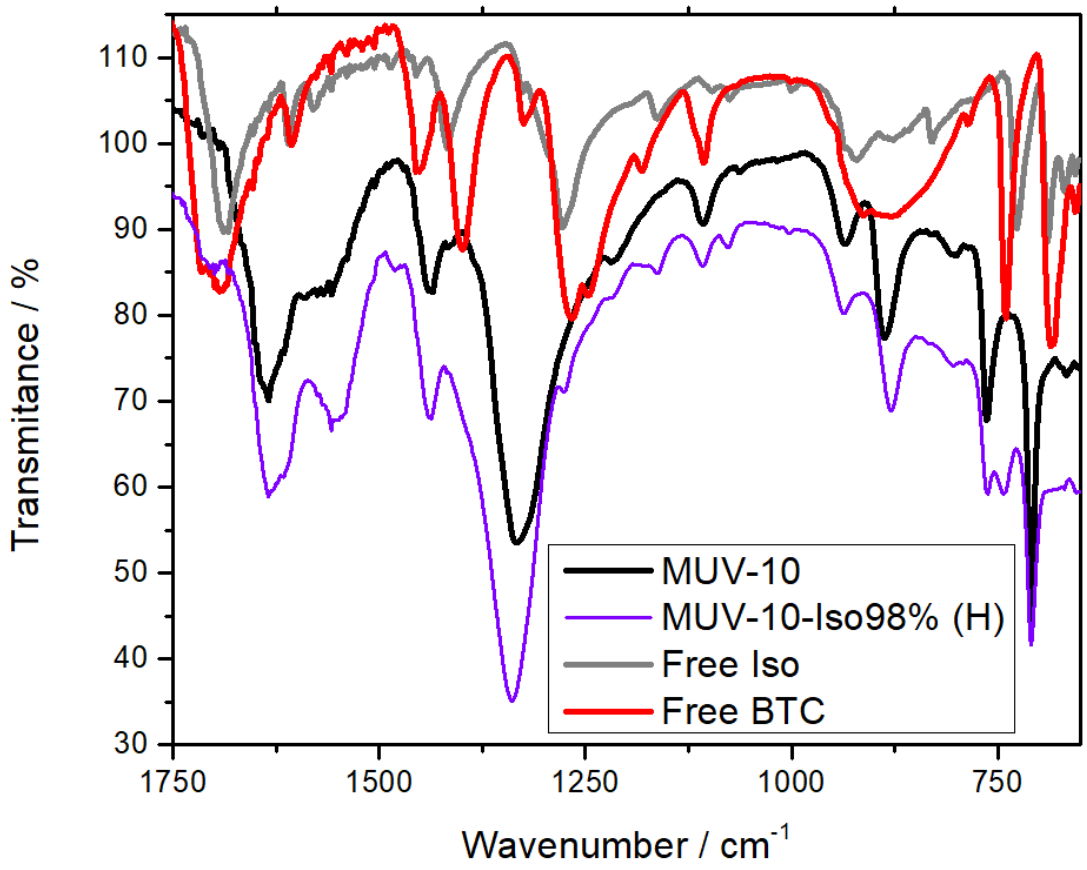

Figure S9: Comparison of the FT-IR profile of iso98%-H with MUV-10-H, free isophthalic acid and free btc, suggesting that the new vibration band at ca. 1700 cm^{-1} for iso98%-H corresponds to free carboxylate groups from btc. The lack of other signals characteristic of free btc suggests that this vibration band is likely due to tangling linkers or to linkers terminating the surface of the MOF.

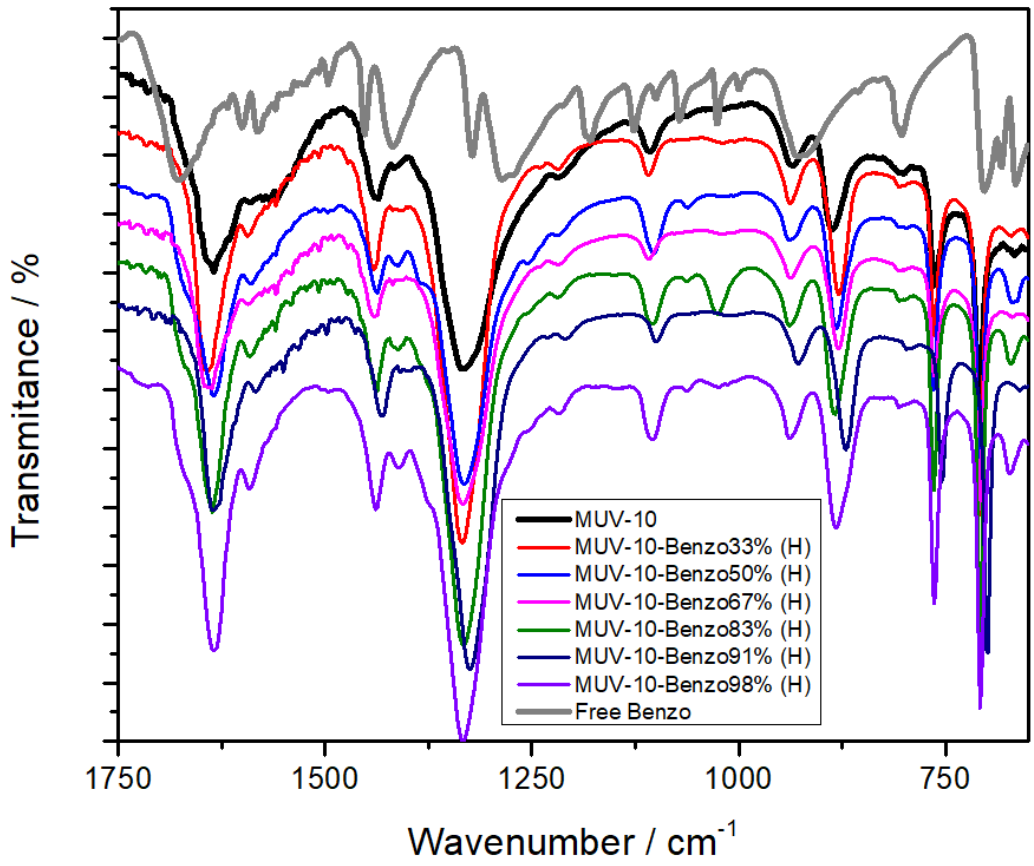

Figure S10: FT-IR of the benzo%-H series compared with MUV-10-H and free modulator, showing characteristic vibration bands from the modulator (ca.1250cm^{-1}) but no free carboxylate vibration band (ca. 1700cm^{-1}), confirming its attachment to the metal clusters.

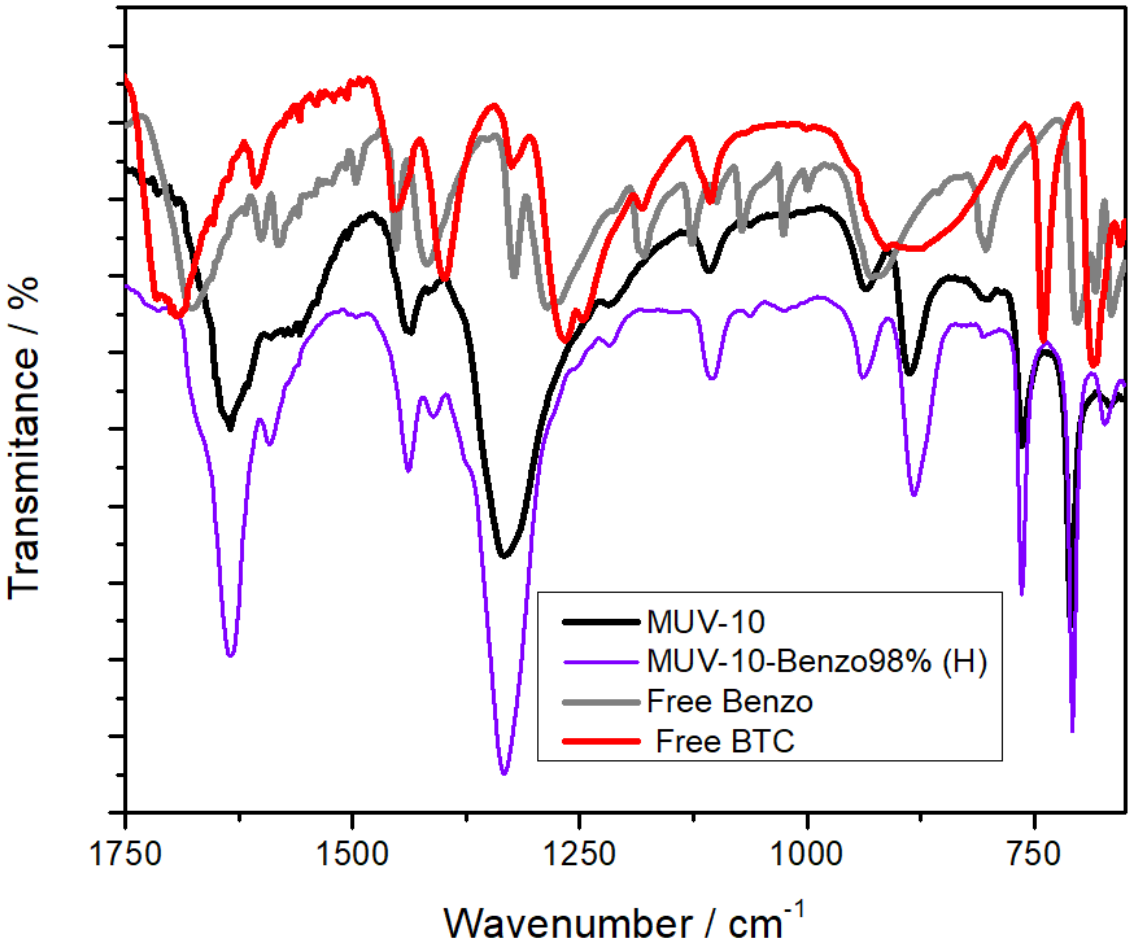

Figure S11: Comparison of the FT-IR profile of benzo98%-H with MUV-10, free benzoic acid and free btc, suggesting that the new vibration band at ca. 1700 cm^{-1} corresponds to free carboxylate groups from btc, similarly to iso98%-H, suggesting tangling linkers or linkers terminating the surface of the MOF.

S.5.3. Molar per cent of metals in MUV-10 iso%-H and benzo%-H

Table S11: Tabulated metal content of iso%-H.

Sample	EDX		ICP	
	% Ca	% Ti	% Ca	% Ti
MUV-10-H	46.70	53.30	46.47	53.53
iso20%-H	45.02	54.98	50.58	49.42
iso33%-H	45.56	54.44	49.43	50.57
iso43%-H	43.98	56.02	43.28	56.72
iso83%-H	43.19	56.81	47.62	52.38
iso91%-H	41.33	58.67	43.85	56.15
iso98%-H	36.77	63.23	46.92	53.08

Table S12: Tabulated metal content of benzo%-H.

Sample	EDX		ICP	
	% Ca	% Ti	% Ca	% Ti
MUV-10 H	46.70	53.30	46.47	53.53
benzo33%-H	42.58	57.42	n/a	n/a
benzo50%-H	38.73	61.27	n/a	n/a
benzo67%-H	43.60	56.40	n/a	n/a
benzo83%-H	42.34	57.66	50.07	49.93
benzo91%-H	45.56	54.44	n/a	n/a
benzo98%-H	55.15	44.85	n/a	n/a

S.5.4. Thermo Gravimetric Analysis MUV-10 iso%-H and benzo%-H

S.5.4.1 Thermo Gravimetric Analysis of iso%-H series.

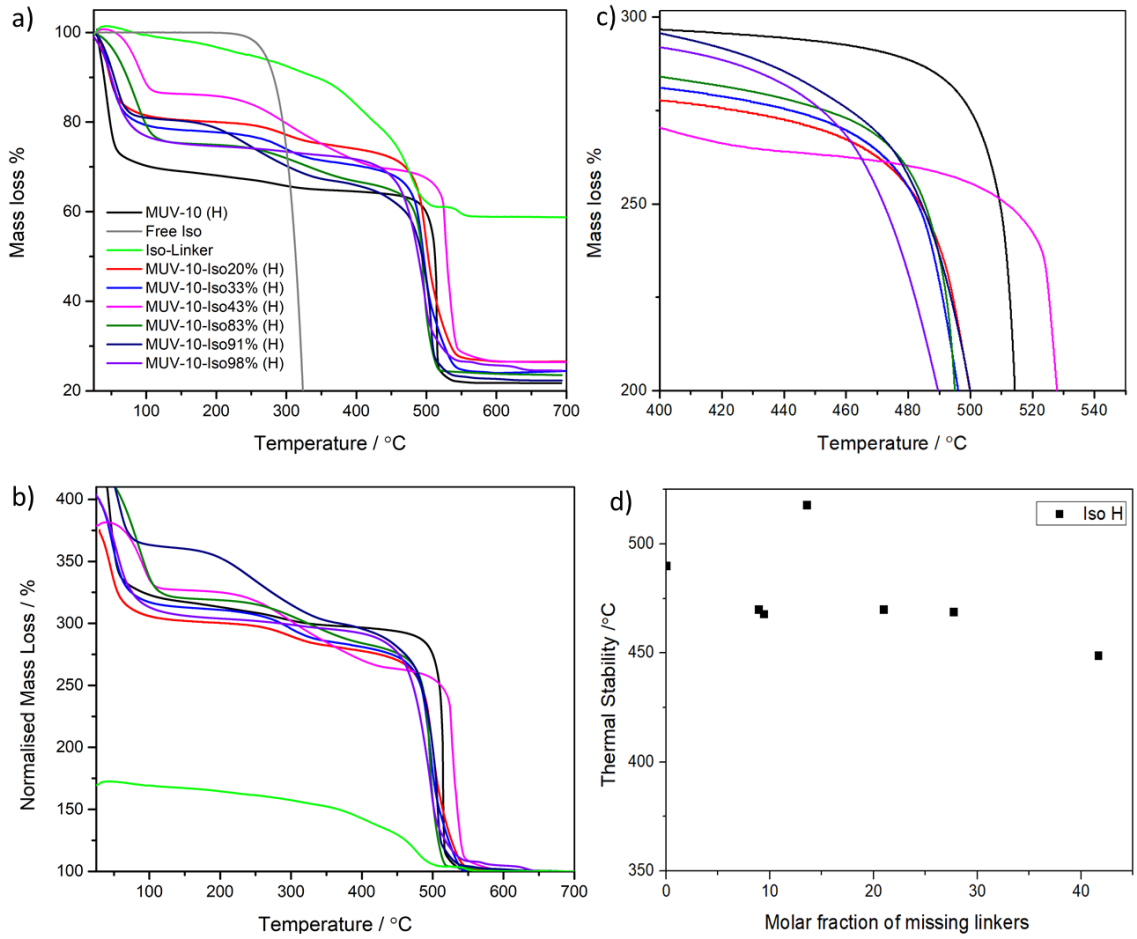

Figure S12: TGA profiles of MUV-10, iso 100% and iso%-H samples normalized to a) the start of the decomposition, b) the mass of the residue and c) zoom of the temperature of the last decomposition step. iso%-H samples display a similar decomposition step to pristine MUV-10. The first decomposition step at approx. 200 ºC is associated to the decomposition of formic acid and increases with the percentage of modulator added to synthesis. The second decomposition step at 450 ºC, is associated to the decomposition of btc and iso ligands in the structure, which is similar to MUV-10-H in magnitude. This –together with the data previously discussed- indicates that iso is partially replacing btc in the structure of MUV-10, with defects compensated by fa and other species such as water/hydroxo pairs. d) Temperature of the last decomposition step as a function of the molar percent of missing linkers, showing a minimum decrease in thermal stability.

From TGA data, and using methodology recently reported by one of us,[13] we have elucidated the composition of the iso%-H series. We have considered three model structures based on previous characterization data: a $TiCaO(H_2O)_W(btc)_X(iso)_y(fa)_z(OH)_D$ MUV-10 defective structure, a mixture of TiO_2 and a MUV-10 defective structure, and a mixture of the iso 100% phase and MUV-10 defective. We have used the experimental ratio between a structure and its residue at different decomposition steps (R_{exp} and R_{expDH}), enclosed in **Table S13,** and the molar ratio between components previously calculated by ^{1}HNMR and ICP. The calculated values for each model are given below.

Table S13: Experimental values obtained from the thermal decomposition profiles of iso%-H.

Sample	R_{exp}	R_{expDH}
MUV-10-H	3.12	2.89
iso20%-H	3.00	2.64
iso33%-H	3.10	2.67
iso43%-H	3.25	2.60
iso83%-H	3.18	2.69
iso91%-H	3.53	2.73
iso98%-H	3.05	2.75

-Model structure: $[TiCaO(H_2O)_W(btc)_X(iso)_y(fa)_z(OH)_D]$:[13]

A small introduction to the application of TGA methodology to MUV-10 is given in Section S.3. The composition of the MOF at each stage of its decomposition profile is given in Figure S13.

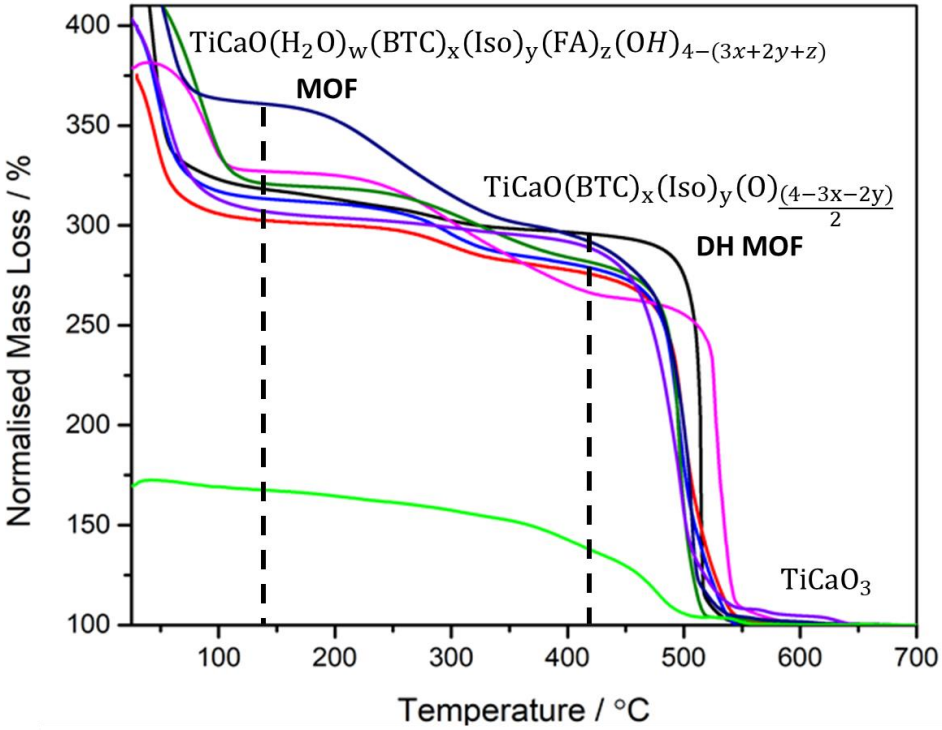

Figure S13: TGA profiles of iso%- H where residues are normalized to 100 %, alongside with the proposed structure of the MOF at each decomposition step for a $TiCaO(H_2O)_W(btc)_X(iso)_y(fa)_z(OH)_D$ model. Legend from Figure S12.

Table S14: Calculated structures $[TiCaO(H_2O)_W(btc)_X(iso)_y(fa)_z(OH)_D]$ of MUV-10-iso H assuming a 1:1 Ti: Ca ratio, enclosing the number of molecules, number and per cent of missing linkers, validation of the calculations with R_{theo} and MUV-10 coordination positions (CP).

Sample	btc	fa	iso	OH	H_20	Missing Linker	ML%	R_{theo}	CP
MUV-10-H	1.403	0.014	0.000	-0.223	2.0	-0.073	-5.25	3.12	13.04
iso20%-H	1.208	0.013	0.016	0.331	2.5	0.122	9.40	3.00	13.16
iso33%-H	1.214	0.024	0.029	0.275	3.1	0.116	8.91	3.10	13.80
iso43%-H	1.153	0.011	0.042	0.448	4.7	0.177	13.53	3.25	15.22
iso83%-H	1.054	0.056	0.245	0.292	3.5	0.276	20.95	3.18	14.17
iso91%-H	0.964	0.098	0.392	0.225	5.8	0.366	27.68	3.53	16.53
iso98%-H	0.778	0.000	0.645	0.378	2.1	0.552	41.65	3.05	12.70

-Model structure: TiO_2@[TiCaO$(H_2O)_w$(btc)$_x$(iso)$_y$(fa)$_z$(OH)$_D$][13]

The composition of the MOF at each stage of its decomposition profile is given in Figure S14. Rearranging the R_{expDH} equation, the number of linkers is obtained, and a similar approach is used to calculate the rest of the components.

$$X\ btc = \frac{\frac{(R_{expDH} - R\%TiO_2) * M_w\ [TiCaO_3])}{R\%MOF} - M_w\ TiCaO - 2 * M_w[O]}{M_w\ [BTC] + nmr * M_w[Iso] - \left(\frac{(3+2nmr)}{2}\right) * M_w[O]}$$

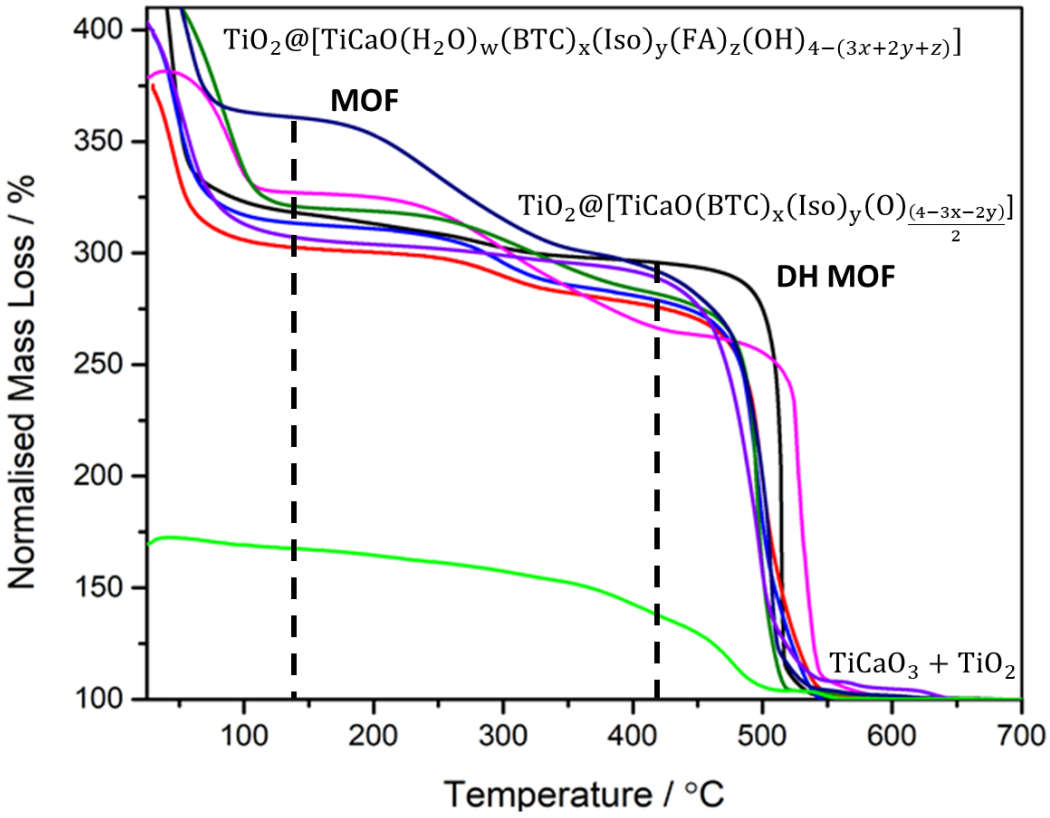

Figure S14: TGA profiles of iso%- H where residues are normalized to 100 %, alongside with the proposed structure of the MOF at each decomposition step for a TiO_2@[TiCaO$(H_2O)_w$(btc)$_x$(iso)$_y$(fa)$_z$(OH)$_D$] model. Legend from Figure S12.

Table S15 shows that if assuming that the extra Titanium comes from TiO_2, MUV-10 H has a ca. 13 % more linker than the pristine structure. In consequence, negative values of OH^- species compensating the charge in the structure are obtained, meaning that the structures will be positively charged. Furthermore, remarkably high water molecules and overall coordination numbers (reaching 21) are determined. Additionally, the defectivity of the samples does not follow any trend with iso incorporation **(Table S16)**. This indicates, that the small extra amount of Titanium might come from the different termination of the crystals, which will also explain why the molar ratio of metals determined by EDX differs from the one determined by ICP.

Table S15: Calculated structures TiO_2@[$TiCaO(H_2O)_W(btc)_X(iso)_y(fa)_z(OH)_D$] of iso%- H assuming that the titanium in excess in comparison to calcium is in the form of TiO_2.

Sample	%R TiO_2	%R MOF	btc	fa	iso	OH	H_20
MUV-10 H	0.072	0.928	1.511	0.015	0.000	-0.548	2.1
iso20%-H	-0.014	1.014	1.192	0.013	0.016	0.380	2.5
iso33%-H	0.013	0.987	1.231	0.024	0.030	0.224	3.3
iso43%-H	0.154	0.846	1.363	0.013	0.049	-0.201	6.2
iso83%-H	0.055	0.945	1.115	0.060	0.260	0.075	5.3
iso91%-H	0.141	0.859	1.123	0.114	0.457	-0.397	9.7
iso98%-H	0.072	0.928	0.838	0.000	0.694	0.099	6.5

Table S16: Calculated structures TiO_2@[$TiCaO(H_2O)_W(btc)_X(iso)_y(fa)_z(OH)_D$] of iso%- H enclosing the number and per cent of missing linkers, validation of the calculations with R_{theo} and the calculated mass fraction of MUV-10 and its coordination positions, resulting in very high numbers that confirm that the extra Titanium is not forming TiO_2.

Sample	Missing Linker	ML%	R_{theo}	Mass fraction MUV-10	Coordination positions
MUV-10 H	-0.178	-13.36	3.12	0.977	13.66
iso20%-H	0.141	10.61	3.00	1.005	13.14
iso33%-H	0.102	7.66	3.10	0.996	14.10
iso43%-H	-0.030	-2.25	3.25	0.953	17.38
iso83%-H	0.218	16.32	3.18	0.983	16.23
iso91%-H	0.210	15.76	3.53	0.960	21.12
iso98%-H	0.495	37.15	3.05	0.977	17.38

-Model structure accounts for a combination of iso 100% and defective MUV-10 phases: iso-Linker@[$TiCaO(H_2O)_W(btc)_X(iso)_y(fa)_z(OH)_D$]

Table 17: Data extracted from TGA profiles of the pure iso-Linker phase.

Rexp iso100 % iso-phase	1.51
iso / Ti (n)	0.275
Oxygen /Ti	1.725
M_w DH isophase exp/calc	120.598 / 120.598
M_w isophase exp/calc	128.584 / 128.584

In order to include the iso-Linker phase as a constant into the TGA analysis of the MOFs composition, the mass fraction of MUV-10 and iso-Linker phase in the residue (denominated R%MOF and R%iso) were calculated as for the previous method, being the residue of MUV-10 $TiCaO_3$ and of the iso-Linker phase TiO_2.

Since the pristine sample has a slightly higher amount of Ti than Ca, the normalized extra Ti% of MUV-10 is subtracted to the normalized extra Ti% of MUV-10-iso, and as the iso-linker phase has traces of Ca, the values are further normalized to its Ti%, hence being the unmodulated sample the 0% and the iso-Linker phase the 100%.

The experimental ratio of the overall framework, which includes both iso-linker phase and MUV-10, and the total residue (given by TGA) is denominated as R_{exp}:

$$R_{exp} = R_{expMOF} * R\%MOF + R_{expisophase} * R\%iso$$

$$R_{expDH} = R_{expDHMOF} * R\%MOF + R_{expDHisophase} * R\%iso$$

Where,

$$R_{expDH} = \left(\frac{M_w\,[DHMOF]}{M_w\,[TiCaO_3]}\right) * R\%MOF + \left(\frac{M_w\,[DH\ iso-Linker\ phase]}{M_w\,[TiO_2]}\right) * R\%iso$$

Using the previously calculated $R_{expDHisophase}$ (from its experimental TGA profile) and R_{expDH}, alongside with the mass fraction of each phase in the residue (R%iso and R%MOF):

$$R_{expDHMOF} = \left(\frac{R_{expDH} - (R_{expDHisoPhase} * R\%iso)}{R\%MOF}\right)$$

Then, since $R_{expDHMOF} = \frac{M_w\,[DH\ MOF]}{M_w\,[TiCaO_3]}$ the molecular weight of MUV-10 can also be calculated to further validate the following calculations of the structure.

Based on ^{1}HNMR analysis we have proposed MUV-10 formula to be as follows: **$TiCaO(H_2O)_W(btc)_X(iso)_y(fa)_z(OH)_D$** where OH is introduced for charge balance.

First, we have calculated based on the dehydrated structures in which only btc and iso remain as ligands, hence using the experimental ratio at T410°C (R_{expDH}), the temperature at which there will be iso linker phase in the form of $Ti(iso)_n(O)_{2-n}$ and MOF in the form of $TiCaO(btc)x(iso)y(O)_{(4-3x-2y)/2}$, as during the previous methodology.

The number of iso coming from the iso-Linker phase can be calculated by using our previously calculated iso/Titanium ratio.

$$(\text{iso})\text{ in phase }(\text{P}) = \%\text{Ti isoPhase} * \text{n}(\frac{\text{iso}}{\text{Ti}}).$$

Where Ti% iso phase is the molar fraction of Ti belonging to the iso-Linker phase in comparison to MUV-10. Then, we can subtract the amount of iso forming the iso-linker phase from the total amount of iso present in the sample, which can be introduced as a function of the linker in order to later rearrange the equation through the molar ratio determined by ^{1}HNMR:

$$\text{iso in MUV} - 10 = \left(\text{nmr}\left(\frac{\text{iso}}{\text{btc}}\right) * \text{xbtc}\right) - \text{iso in isoPhase(P)}$$

Substituting this in the experimental ratio between MUV-10 and its residue (previously calculated assuming a constant iso-Linker phase structure) results in btc determination within the MUV-10 structure, which then leads to the calculation of the other moieties as previously detailed.

$$\text{R}_{\text{expDHMOF}} = \left(\frac{\text{M}_\text{w}\,[\text{TiCaO(btc)}_\text{x}(\text{iso})_{(\text{x}*\text{nmr}-\text{P})}(\text{O})_{\frac{(4-3\text{x}-2*(\text{x}*\text{nmr}-\text{P}))}{2}}]}{\text{M}_\text{w}\,[\text{TiCaO}_3]}\right)$$

$$\text{R}_{\text{expDHMOF}} = \left(\frac{\text{M}_\text{w}\,[\text{TiCa0}]+\text{x}*\text{M}_\text{w}\,[\text{btc}]+(\text{x}*\text{nmr}-\text{P})*\text{M}_\text{w}\,[\text{iso}]+\frac{(4-3\text{x}-2*(\text{x}*\text{nmr}-\text{P}))}{2}*\text{M}_\text{w}\,[\text{O}]}{\text{M}_\text{w}\,[\text{TiCaO}_3]}\right)$$

Rearranging the equation,

$$\text{x btc} = \left(\frac{\text{R}_{\text{expDHMOF}} *\ \text{M}_\text{w}\,[\text{TiCaO}_3] - \text{M}_\text{w}\,\text{TiCa0} + \text{P} * \text{M}_\text{w}\,[\text{iso}] - 2 * \text{M}_\text{w}\,[\text{O}] + \text{P} * \text{M}_\text{w}\,[\text{O}]}{\text{M}_\text{w}\,[\text{btc}] + \text{nmr} * \text{M}_\text{w}\,[\text{iso}] - \frac{3+2\text{nmr}}{2} * \text{M}_\text{w}\,[\text{O}]}\right)$$

Once x is obtained, the number of iso in MUV-10 can be obtained applying the previously discussed formula:

$$\text{iso in MUV} - 10\ (\text{N}) = \left(\text{nmr}\left(\frac{\text{iso}}{\text{btc}}\right) * \text{xbtc}\right) - \text{iso in isoPhase(P)}$$

Based on the previously discussed ^{1}HNMR ratio the fa content can be obtained as a function of btc, being $\text{Z} = \text{X} * \text{NMR}\,(\frac{\text{fa}}{\text{btc}})$.

The values are tabulated in **Table S18**, alongside with calculation of charge provided by the anions in the MUV-10 having to compensate for Ti and Ca as follows:

$Ti^{4+} + Ca^{2+} = O^{2-} + xbtc^{3-} + niso^{2-} + zfa^{-} + DOH^{-}$

In cases in which the charge is not fully compensated by the present species, the number of OH^- species needed to compensate the charge are calculated using the following equation:

$$4\mathrm{Ti} + 2\mathrm{Ca} = 2\mathrm{O} + 3\mathrm{Xbtc} + 2(\mathrm{XRnmriso} - \mathrm{P}) + * \mathrm{XRnmrfa} + \mathrm{D\ OH},$$

Hence,

$$\mathrm{D\ OH} = 4 + 2\mathrm{P} - \mathrm{X}(3\mathrm{btc} + 2\mathrm{Rnmriso} + \mathrm{Rnmrfa})$$

To calculate the number of water molecules a similar approach is employed. Since

$$\mathrm{R_{exp}} = \left(\frac{\mathrm{M_w\ [MOF]} + \mathrm{w} * \mathrm{M_w\ [H_2O]}}{\mathrm{M_w\ [TiCaO_3]}}\right) * \mathrm{R\%MOF} + \left(\frac{\mathrm{M_w\ [iso - Linker\ phase]}}{\mathrm{M_w\ [TiO_2]}}\right) * \mathrm{R\%Iso}$$

Then

$$\mathrm{w\ M_w\ [H_2O]} = \frac{\frac{(\mathrm{R_{exp}} - \mathrm{R_{expisoPhase}} * \mathrm{R\%iso}) *\ \mathrm{[TiCaO_3]}}{\mathrm{R\%MOF}} - \mathrm{M_w[MOF]}}{\mathrm{M_w\ [H_2O]}}$$

Once the MOF structure is determined, its molecular weight can be used to determine the mass fraction of MUV-10 and iso-phase (S%MOF and S%iso) in the overall structure.

$$\mathrm{S\%MOF} = \left(\frac{\mathrm{M_w\ [MOF] * Molar\ fraction\ (Ti)\ MOF}}{(\mathrm{M_w\ [MOF] * Molar\ fraction\ (Ti)\ MOF + M_w\ [iso-Linker] * Molar\ fraction\ (Ti)\ iso-Linker\ phase\ )}}\right)$$

Tables S18 and **S19** show the tabulated values for the determination of MUV-10 structure within the iso-Linker phase@MUV-10 composite for MUV-10-iso H, alongside with the mass fraction of iso-Linker phase (R%iso) in the residue ($TiCaO_3$ and TiO_2).

Table S18: Tabulated values extracted from the analysis of the thermogravimetric profiles of MUV-10-iso H using the previously discussed formulas based on the ratios between the frameworks and their residues, given in Table S13, normalizing the extra Titanium per cent to their mass residues. The number of molecules (either btc, iso or fa correspond to the estimates structure $[TiCaO(H_2O)_w(btc)_x(iso)_y(fa)_z(OH)_D]$ of the Iso-Linker@MUV-10 Composite, in which if defect-free there are 1.33 btc linkers.

Sample	%R iso	P iso in iso-linker	btc	fa	iso	OH	H_20
MUV-10 H	0	N/A	1.403	0.015	0	-0.237	1.67
iso20%-H	-0.085	0.000	1.282	0.014	0.017	0.105	1.61
iso33%-H	-0.062	0.000	1.291	0.025	0.031	0.041	2.10
iso43%-H	0.099	0.044	1.241	0.012	0.001	0.263	4.04
iso83%-H	-0.022	0.000	1.087	0.055	0.253	0.177	2.89
iso91%-H	0.081	0.036	1.031	0.095	0.384	0.043	4.06
iso98%-H	-0.006	0.000	0.785	0.008	0.651	0.335	1.73

*Note that the extra ti% has been corrected with MUV-10-H values, resulting in some cases as negative values, which have been included as 0 during the calculations.

Table S19: Calculated values for iso-Linker@[$TiCaO(H_2O)_W(btc)_X(iso)_y(fa)_z(OH)_D$] from iso%- H , enclosing number and per cent of missing linkers, validation of the calculations with R_{theo} and the calculated mass fraction of the iso-Linker and of MUV-10.

Sample	Missing Linker	ML %	R_{theo}	Coordination positions	Mass fraction iso-phase	Mass fraction MUV-10
MUV-10 H	-0.073	-5.2	3.12	12.89	0	1
iso20%-H	0.051	3.80	3.00	12.50	0.000	1.000
iso33%-H	0.042	3.16	3.10	13.06	0.000	1.000
iso43%-H	0.092	6.92	3.25	14.78	0.052	0.948
iso83%-H	0.246	18.43	3.18	13.71	0.000	1.000
iso91%-H	0.302	22.64	3.53	15.02	0.040	0.960
iso98%-H	0.548	41.08	3.05	12.39	0.000	1.000

The values obtained by the different models show that defective $TiCaO(H_2O)_W(btc)_X(iso)_y(fa)_z(OH)_D$ is the best structural match. Although the extra per cent of Ti is low (ca. 5% maximum), as it does not decompose during the TGA profiles it highly affects the structure composition if assumed that it is forming TiO_2, resulting in remarkably high coordination numbers that indicate that there is no plausible way that it comes from TiO_2 formation. Structural composition does not change drastically if it is assumed that the extra Ti comes from the formation of the iso100% phase, but higher coordination numbers than for the pure phase defective structure are obtained, indicating together with FT-IR and with the TGA profiles that iso100% this is not a good model.

S.5.4.2 Thermo Gravimetric Analysis of benzo%-H series.

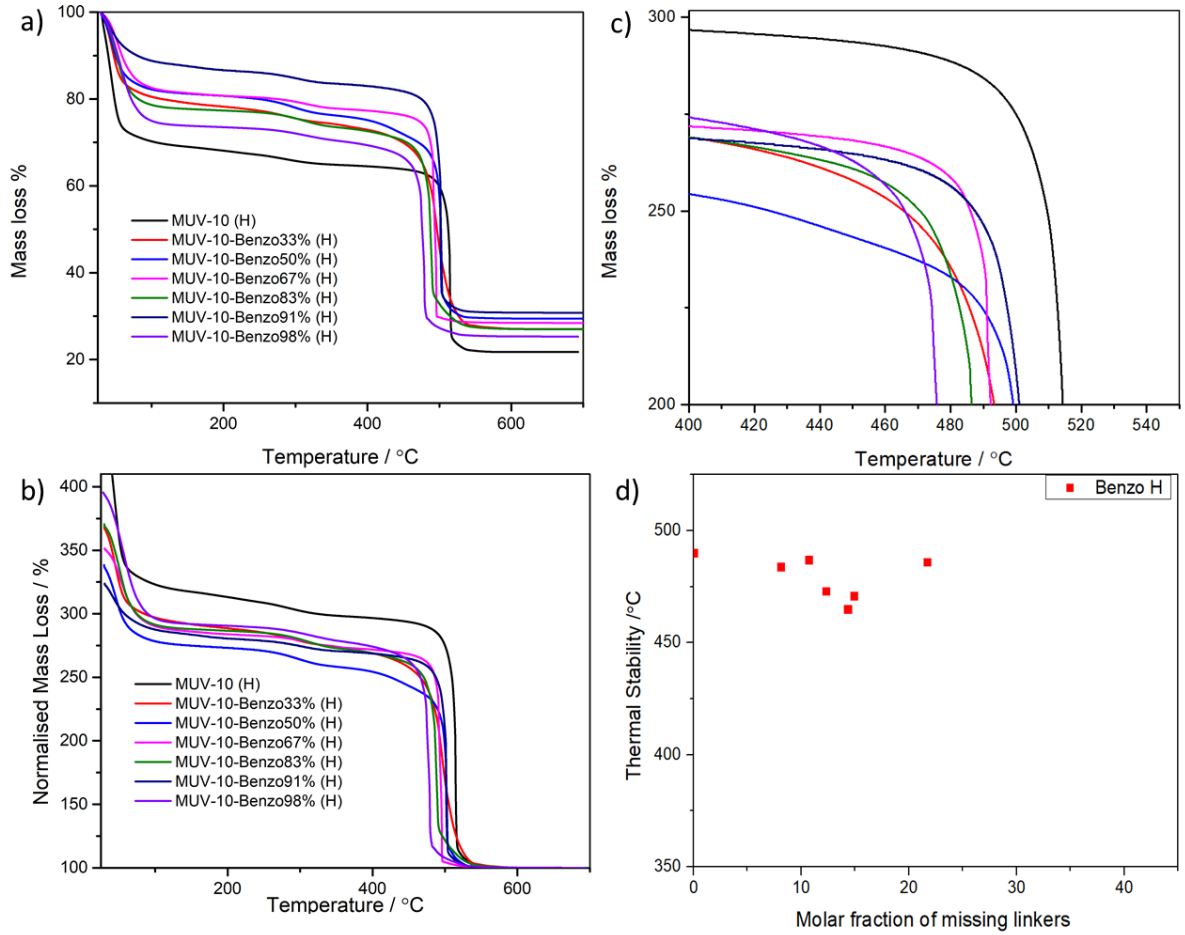

Figure S15: TGA profiles of MUV-10 and benzo%-H samples normalized to a) the start of the decomposition and b) the mass of the residue. c) zoom of the temperature of the last decomposition step. d) Temperature of the last decomposition step as a function of the molar percent of missing linkers, showing a minimum decrease in thermal stability.

Table S20: Tabulated values of the experimental MOF/residue ratio of benzo%-H samples.

Sample	R_{exp}	R_{expDH}
MUV-10	3.12	2.89
benzo33%-H	2.89	2.53
benzo50%-H	2.73	2.41
benzo67%-H	2.85	2.66
benzo83%-H	2.87	2.60
benzo91%-H	2.82	2.65
benzo98%-H	2.88	2.59

Table S21: Tabulated calculations of the number of btc, benzo and missing linker based on the experimental MOF/residue ratio of benzo%-H for a **defective $[TiCaO(H_2O)_W(btc)_X(benzo)_y(fa)_z(OH)_D]$** MOF structure.

Sample	btc	fa	benzo	OH	H_20	ML	ML%	CP
MUV-10	1.403	0.014	0.000	-0.223	2.0	-0.073	-5.2	13.04
benzo33 %-H	1.135	0.024	0.002	0.570	2.4	0.199	14.9	12.81
benzo50 %-H	1.045	0.010	0.003	0.853	2.0	0.289	21.7	12.11
benzo67 %-H	1.226	0.089	0.011	0.224	1.1	0.108	8.1	11.92
benzo83 %-H	1.169	0.031	0.030	0.432	1.8	0.164	12.3	12.33
benzo91 %-H	1.191	0.031	0.054	0.341	1.0	0.142	10.7	11.71
benzo98 %-H	1.142	0.056	0.061	0.455	1.8	0.191	14.3	12.39

Table S22: Tabulated calculations of the number of btc, benzo and missing linker based on the experimental MOF/residue ratio of benzo%-H for a defective **TiO_2@[$TiCaO(H_2O)_W(btc)_X(benzo)_y(fa)_z(OH)_D$]** MOF structure, with Ti content calculated by EDX. The calculated btc exceeds the number of linker in the pristine structure, with consequent negative OH- ligands compensating for the positive charge. This, together with the fact that ICP analysis differed from EDX measurements, showing great Ti/Ca ratios, brought us to use the $[TiCaO(H_2O)_W(btc)_X(benzo)_y(fa)_z(OH)_D]$ model for further analysis. Although the mass fraction of TiO_2 ($S\%TiO_2$) is small (max. 9 mass%), its impact in TGA analysis is noticeable, as it does not decompose and alters the materials profiles significantly. Additionally, despite EDX measurements indicate a higher Ti content, ICP revealed 50.1 Ti% while EDX determined a 57. Ti%.

Sample	$R\%TiO_2$	btc	fa	benzo	OH	H_20	ML%	CP	$S\%\ TIO_2$
MUV-10	0.072	1.511	0.015	0.000	-0.548	2.1	-13.98	13.66	0.023
benzo3 3%-H	0.170	1.367	0.030	0.002	-0.135	3.3	-2.55	14.422	0.059
benzo5 0%-H	0.255	1.402	0.014	0.005	-0.228	3.3	-5.15	14.572	0.093
benzo6 7%-H	0.147	1.437	0.104	0.012	-0.440	1.7	-7.80	13.177	0.052
benzo8 3%-H	0.175	1.417	0.037	0.037	-0.363	2.7	-6.33	14.084	0.061
benzo9 1%-H	0.103	1.328	0.035	0.061	-0.139	1.7	0.40	12.806	0.036
benzo9 8%-H	-0.123	1.017	0.050	0.054	0.790	1.7	23.69	11.875	-0.043

S.5.5. Computational simulations of defective MUV-10 phases.

S.5.5.1 Defect energetics

To simulate defective MUV-10 phases, both the lattice parameter and atomic position of pristine MUV-10 were relaxed. Then, one btc per unit cell was manually exchanged by a modulator (iso, benzo, AcOH or fa) and enough OH^- anions for overall charge compensation. Next, atomic positions were further relaxed keeping the lattice parameters constant.

$$(\mathrm{TiCaO})_6(btc)_8 + mod + \ (H_2O)_{1\ or\ 2} = \ (\mathrm{TiCaO})_6(btc)_7(mod)(OH)_{1\ or\ 2} + \ btc$$

The energy balance required for introducing a missing linker in MUV-10 was calculated via:

$$E = E_{(\mathrm{TiCaO})_6(btc)_7(mod)(OH)_{1\ or\ 2}} + E_{btc} - \ E_{(\mathrm{TiCaO})_6(btc)_8} - E_{mod} - (1\ or\ 2)\ E_{H_2O}$$

Table S23: Energy balance E(eV) required for replacing one btc in MUV-10 by a iso, benzo, AcOH or fa molecule.

molecule	E(eV)
Iso	-1.45
benzo	-1.09
AcOH	-0.65
fa	-1.06

S.6. MUV-10 modulation in linker deficient conditions: characterization of MUV-10 iso%-L samples.

S.6.1 PXRD of MUV-10 iso%-L.

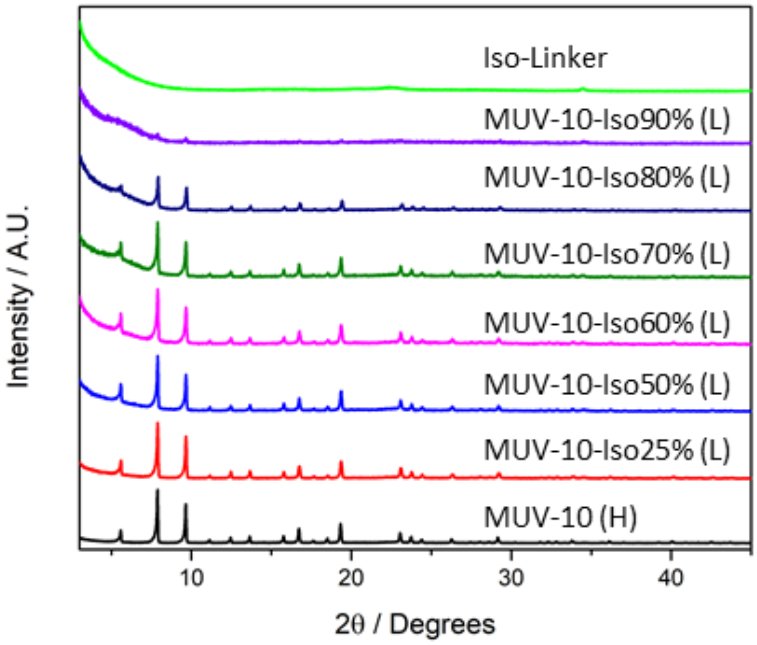

Figure S16: PXRD pattern of iso%-L series showing a remarkable increase in intensity at low reflection angles associated with a decrease in crystallinity, when the quantity of isophthalic acid added to the synthetic mixture increases, suggesting the formation of the iso 100% phase.

S.6.2 Incorporation of modulators in MUV-10 iso%-L as estimated with ^{1}H-NMR.

Table S24: Tabulated ^{1}H-NMR data from acid digested iso%-L series, showing the modulator content increasing with the addition of modulator.

Sample	iso mol %	fa mol %	iso ratio	fa ratio
iso25%-L	9.12	10.75	0.100	0.120
iso50%-L	19.54	24.83	0.243	0.330
iso60%-L	22.39	12.61	0.288	0.144
iso70%-L	33.15	40.28	0.496	0.674
iso80%-L	41.27	20.19	0.703	0.253
iso90%-L	64.38	56.54	1.807	1.301

S.6.3 FT-IR of MUV-10 iso%-L.

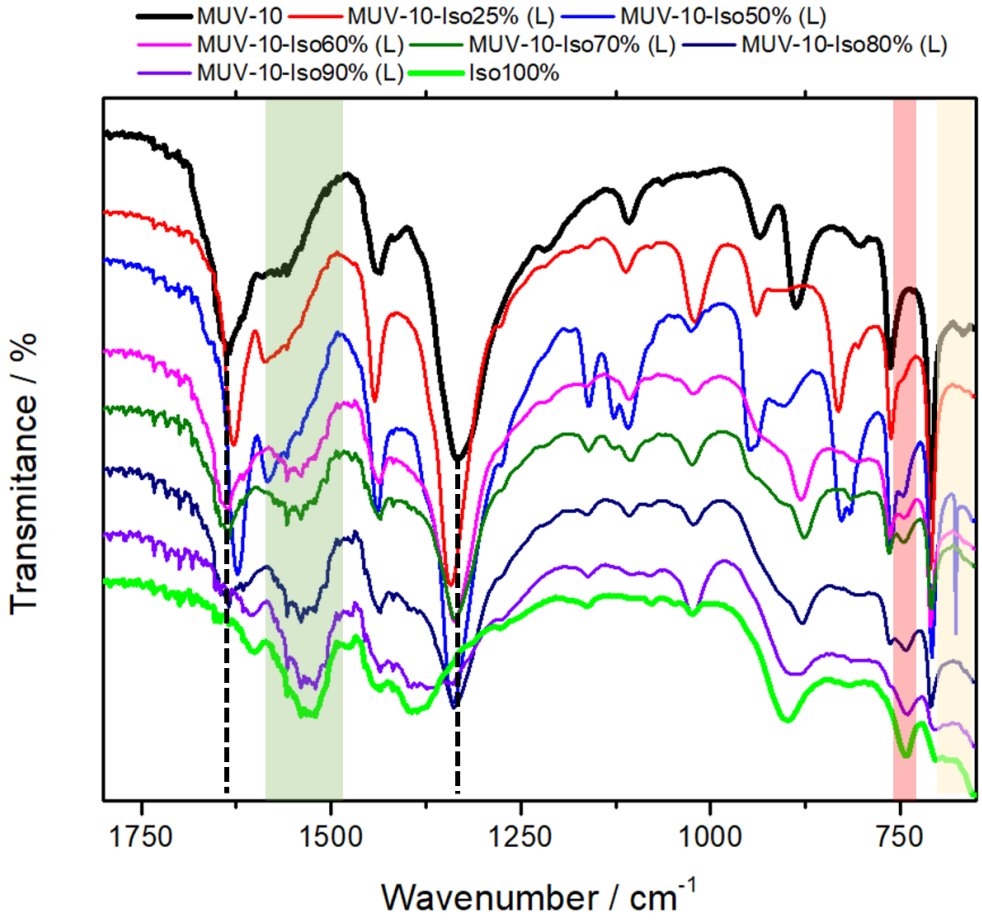

Figure S17: Comparison of FT-IR profiles of MUV-10-H, iso 100% and iso%-L series showing characteristic vibration bands from the last but no free carboxylate vibrations (1700 cm^{-1}, Figure S9) confirming modulator's attachment to the metal clusters. A gradual shift towards the iso 100% phase carboxylate (green) and metallic vibration bands (yellow) is apparent since the addition of small quantities of modulator, whereas changes in the esqueleton vibration band at 742 cm^{-1} (red) are less significant than for iso%-H phases (Figure S8), suggesting the last band to be an indicator of Is incorporation, but not exclusively of the iso 100% phase. Shifting in the two major MUV-10 vibration bands (dashed) are observed, suggesting that MUV-10 and iso 100% phases are intergrowing and not only forming as independent frameworks.

S.6.4. Molar per cent of metals in MUV-10 iso%-L

Table S25: Tabulated metal content of iso%-L series.

Sample	EDX		ICP	
	% Ca	% Ti	% Ca	% Ti
MUV-10 H	46.70	53.30	46.47	53.53
iso25%-L	37.28	62.72	n/a	n/a
iso50%-L	27.5	72.5	n/a	n/a
iso60%-L	25.99	74.01	n/a	n/a
iso70%-L	20.75	79.25	21.81	78.19
iso80%-L	16.65	83.35	n/a	n/a
iso90%-L	3.42	96.58	4.62	95.38

This indicates, in great agreement with previous FT-IR discussion, that iso 100% phase (formed of Ti and iso) forms along with MUV-10 phase in the MUV-10 iso%-L series.

S.6.5. Thermo Gravimetric Analysis of MUV-10 iso%-L.

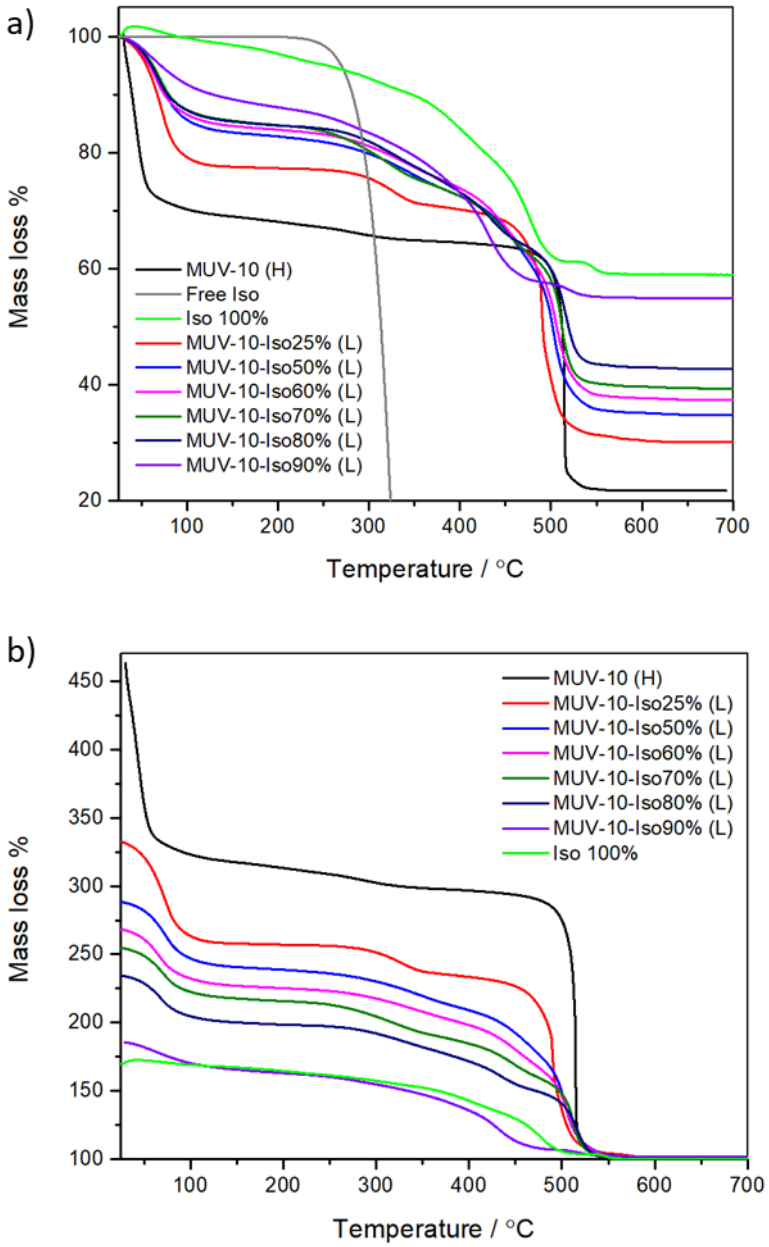

Figure S18: TGA profiles of MUV-10, iso 100% and iso%-L samples normalized to a) the start of the decomposition, b) the mass of the residue. The formation of the amorphous phase 'iso100%', which thermal decomposition is more gradual than MUV-10, is translated to the thermal decomposition profiles of the iso%-L series, in which a decrease in thermal stability, with more gradual decomposition profiles, is observed. However, the gradual decomposition does not allow to accurately determine the temperature of the last decomposition step.

-Model structure: $[TiCaO(H_2O)_W(btc)_X(iso)_y(fa)_z(OH)_D]$:[13]

The calculations are performed using the model detailed in S.5.4.

Table S26: Calculated structures $[TiCaO(H_2O)_W(btc)_X(iso)_y(fa)_z(OH)_D]$ by assuming a 1:1 Ti: Ca ratio, enclosing the number of molecules, number and per cent of missing linkers, validation of the calculations with R_{theoDH} and MUV-10 coordination positions, showing a drastic decrease in the coordination positions that confirms that the samples are not only defective MUV-10.

Sample	btc	fa	iso	OH	H_20	Missing Linker	ML%	R_{theoDH}	CP
MUV-10	1.403	0.014	0.000	-0.223	2.0	-0.073	-5.25	2.89	13.04
iso25%-L	0.934	0.112	0.094	0.899	0.8	0.396	29.94	2.36	10.93
iso50%-L	0.726	0.240	0.176	1.230	0.3	0.604	45.53	2.17	10.10
iso60%-L	0.638	0.092	0.184	1.626	0.4	0.692	52.13	2.06	9.73
iso70%-L	0.482	0.325	0.239	1.750	0.2	0.848	63.82	1.91	9.44
iso80%-L	0.383	0.097	0.269	2.214	0.0	0.947	71.22	1.81	8.76
iso90%-L	0.099	0.128	0.291	2.994	-0.6	1.231	92.58	1.45	7.45

-Model structure: TiO_2@[$TiCaO(H_2O)_W(btc)_X(iso)_y(fa)_z(OH)_D$][13]

The calculations are performed using the model detailed in **S.5.4.**

Tables S27 and **S28** show the tabulated values obtained by assuming that the extra Titanium (compared to Calcium) is forming TiO_2, showing remarkably high negative values for OH^- defect compensating species, (with consequently a drastically high number of water coordinated molecules) in addition to a remarkably high presence of btc (pristine or higher than pristine) and a subsequent high amount of iso in the structure. This leads to impossible coordination numbers (reaching 75 coordination positions) and shows that there is no plausible way that the extra titanium will be coming from the formation of TiO_2.

Table S27: Calculated structures TiO_2@[$TiCaO(H_2O)_W(btc)_X(iso)_y(fa)_z(OH)_D$] by assuming that the titanium in excess in comparison to calcium is in the form of TiO_2.

Sample	%R TiO_2	%R MOF	btc	fa	iso	OH	H_20
MUV-10	0.072	0.928	1.511	0.01511	0.000	-0.548	2.1
iso25%-L	0.286	0.714	1.308	0.15750	0.131	-0.344	2.7
iso50%-L	0.490	0.510	1.424	0.47034	0.346	-1.433	4.6
iso60%-L	0.520	0.480	1.331	0.19190	0.384	-0.951	5.2
iso70%-L	0.624	0.376	1.281	0.86367	0.635	-1.976	7.6
iso80%-L	0.702	0.298	1.286	0.32520	0.903	-1.989	9.9
iso90%-L	0.941	0.059	1.677	2.18268	4.948	-13.11	51.7

Table S28: Calculated structures enclosing the number and per cent of missing linkers, validation of the calculations with R_{theo} and the calculated mass fraction of MUV-10 and its coordination positions.

Sample	Missing Linker	ML %	R_{theo}	Mass fraction MUV-10	Coordination positions
MUV-10	-0.178	-13.33	3.12	0.977	13.66
iso25%-L	0.025	1.89	2.56	0.888	14.08
iso50%-L	-0.090	-6.78	2.36	0.792	17.03
iso60%-L	0.003	0.21	2.24	0.768	17.13
iso70%-L	0.053	3.95	2.14	0.709	20.54
iso80%-L	0.048	3.57	1.98	0.646	22.94
iso90%-L	-0.344	-25.81	1.61	0.415	75.85

-Model structure accounts for a combination of iso 100% and defective MUV-10 phases: iso-Linker@[$TiCaO(H_2O)_W(btc)_X(iso)_y(fa)_z(OH)_D$]

As envisioned in the representation of the TGA profiles **(Figure S18)**, in MUV-10-iso 90% either MUV-10, the iso-Linker phase or both are highly defective, and its composition cannot be calculated. In the rest of the samples, both the mass fraction of the iso-Linker phase and MUV-10 defectivity increase with iso addition, as tabulated in **Tables S29** and **S30**. MUV-10 coordination positions are close to 13 in all cases, indicating a good fit between the real structure and the proposed model.

Table S29: Tabulated values extracted from the analysis of the thermogravimetric profiles by using the previously discussed formulas based on the ratios between the frameworks and their residues, normalizing the extra Titanium per cent to their mass residues. The number of molecules (either btc, iso or fa correspond to the estimated structure [$TiCaO(H_2O)_W(btc)_X(iso)_y(fa)_z(OH)_D$].

Sample	%R iso	P	btc	fa	iso	OH	H_20
MUV-10	0	N/A	1.403	0.000	0.014	-0.237	2.0
iso25%-L	0.290	0.113	1.254	0.151	0.013	0.061	1.50
iso50%-L	0.497	0.172	1.228	0.406	0.126	-0.343	1.67
iso60%-L	0.528	0.180	1.106	0.160	0.139	0.244	1.83
iso70%-L	0.633	0.205	0.933	0.629	0.258	0.055	2.56
iso80%-L	0.712	0.222	0.811	0.205	0.348	0.666	2.45
iso90%-L	0.957	0.268	-0.101	-0.132	-0.567	5.570	7.78

Table S30: Calculated structures enclosing number and per cent of missing linkers, validation of the calculations with R_{theo} and the calculated mass fraction of the iso 100% and MUV-10 phases.

Sample	ML	ML %	R_{theo}	CP	Mass fraction iso-Linker	Mass Fraction MUV-10	Fraction of iso in iso-Linker
MUV-10	-0.073	-5.25	3.12	13.04	0	1	0
iso25%-L	0.079	5.93	2.56	12.44	0.182	0.818	0.896
iso50%-L	0.105	7.85	2.36	13.01	0.339	0.661	0.578
iso60%-L	0.227	17.00	2.24	12.59	0.379	0.621	0.565
iso70%-L	0.400	29.98	2.14	13.51	0.476	0.524	0.443
iso80%-L	0.522	39.14	1.98	12.79	0.579	0.421	0.390

iso90%-L	1.434	107.58	1.61	13.21	0.957	0.043	-0.895

S.7. MUV-10 modulation in linker deficient conditions: characterization of MUV-10 benzo%-L samples.

S.7.1 PXRD of MUV-10 benzo%-L.

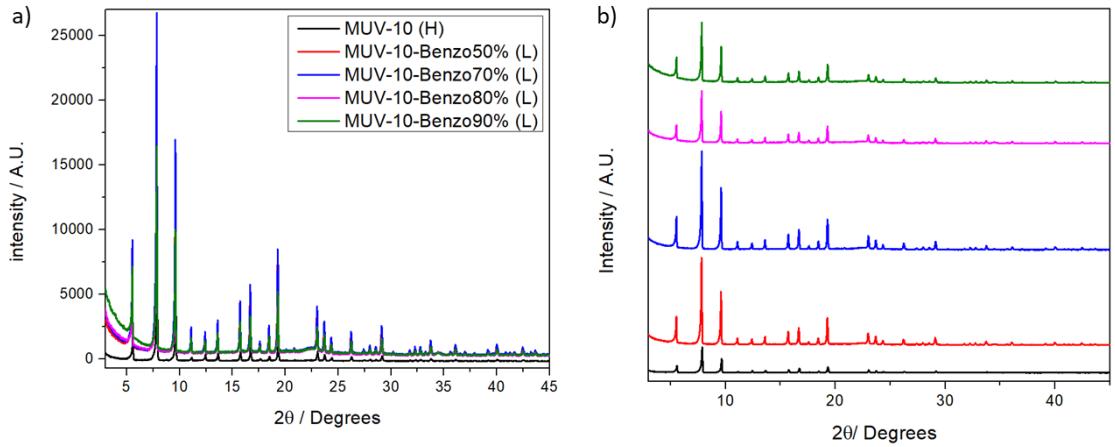

Figure S19: PXRD patterns of benzo%-L series showing high crystallinity and phase purity. It is worth noting that an increase in the intensity of the diffraction lines at low reflection angles is observed for increasing quantities of benzoic acid added to the synthetic mixture.

S.7.2 Incorporation of modulators in MUV-10 benzo%-L as estimated with ^{1}H-NMR.

Table S31: Tabulated data extracted from acid digested ^{1}HNMR of benzo%-L series, showing benzo and formic acid content increasing with the addition of modulator.

Sample	benzo mol %	fa mol %	benzo ratio	fa ratio
benzo25%-L	0.971	15.106	0.010	0.178
benzo50%-L	1.255	18.078	0.013	0.221
benzo70%-L	1.807	12.764	0.018	0.146
benzo80%-L	2.994	19.304	0.031	0.239

S.7.3 FT-IR of MUV-10 benzo%-L.

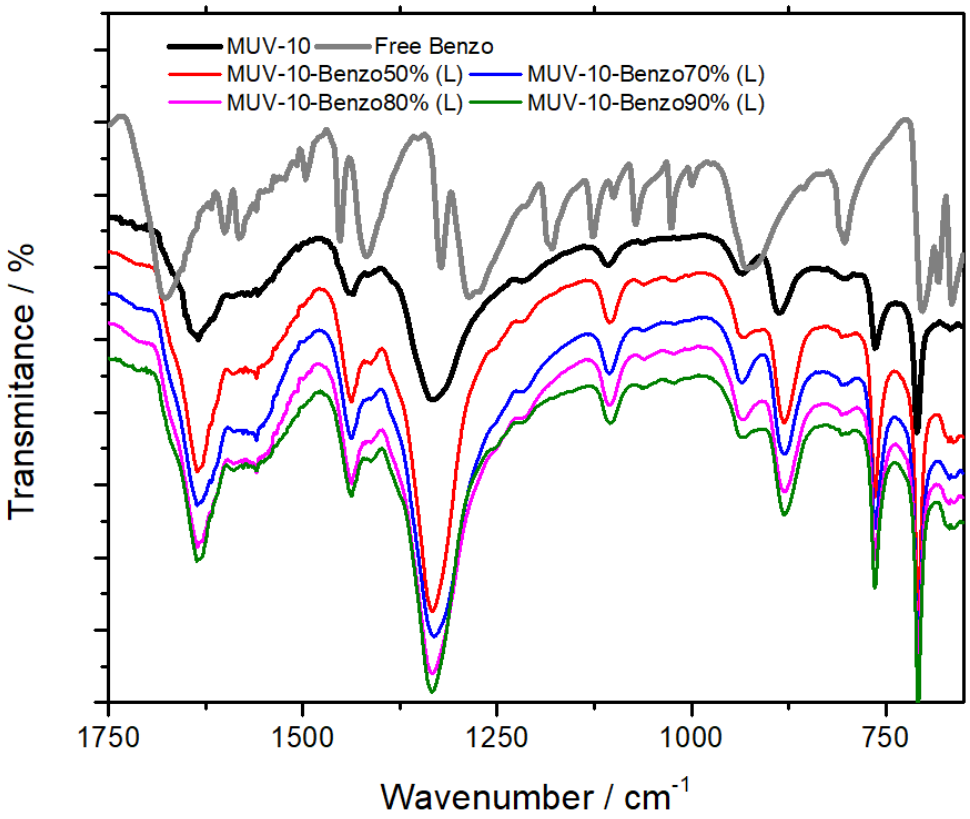

Figure S20: FT-IR of benzo%- L compared with MUV-10-H and free modulator, showing no free carboxylate vibration band (ca. 1700cm^{-1}) and changes in the metal vibration bands at ca. 650 cm^{-1}, confirming its attachment to the metal clusters.

S.7.4. Molar per cent of metals in MUV-10 benzo%-L.

Table S32: Tabulated metal content of benzo%-L series.

Sample	EDX		ICP	
	% Ca	% Ti	% Ca	% Ti
MUV-10 H	46.70	53.30	46.47	53.53
benzo25%-L	41.40	58.60	n/a	n/a
benzo50%-L	41.59	58.41	n/a	n/a
benzo70%-L	40.62	59.38	n/a	n/a
benzo80%-L	34.65	65.35	40.041	59.959

S.7.5. Thermo Gravimetric Analysis MUV-10 benzo%-L series

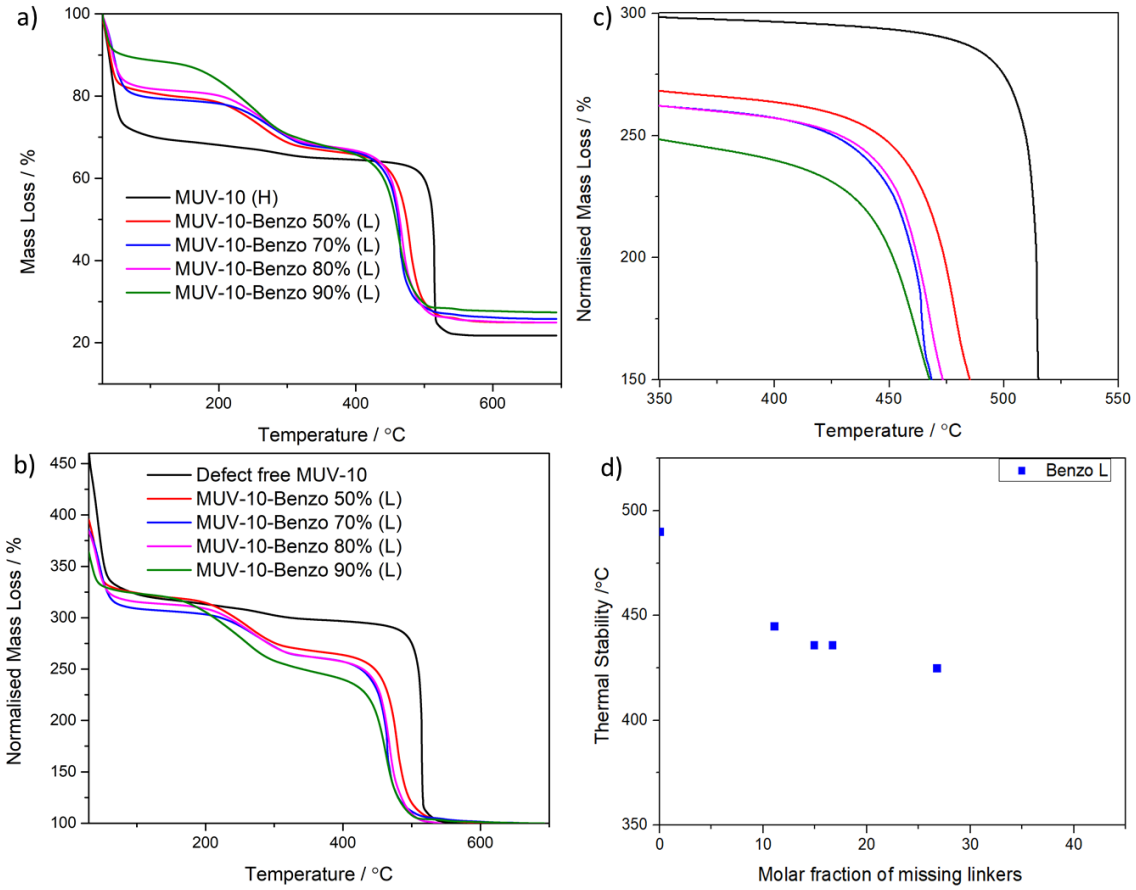

Figure S21: Representation of the TGA profile of benzo%-L series. A) Normalised to starting mass a 100%, showing higher metal content and b) normalised to residue as a 100%, a lower linker decomposition profile step and a higher per cent of defect-compensating species. c) zoom of the temperature of the last decomposition step. d) Temperature of the last decomposition step as a function of the molar percent of missing linkers, showing a decrease in thermal stability related to the sample's defectivity.

The same calculations performed for benzo%-H phases (Section S.5.4) were applied to the benzo%-L series yielding the information presented below:

-Model structure: $[TiCaO(H_2O)_W(btc)_X(iso)_y(fa)_z(OH)_D]$:[13]

Table S33: Tabulated calculations of benzo%-L composition on the experimental MOF/residue ratio by assuming this model.

Sample	R_{exp}	R_{expDH}	btc	fa	benzo	OH	H_20
MUV-10	3.12	2.89	1.403	0.014	0.000	-0.223	2.0
benzo25%-L	3.10	2.61	1.186	0.211	0.012	0.220	3.2
benzo50%-L	3.04	2.54	1.135	0.250	0.014	0.331	3.1
benzo70%-L	3.07	2.51	1.111	0.163	0.020	0.484	3.6
benzo80%-L	3.10	2.34	0.977	0.234	0.030	0.806	4.8

Table S34: Tabulated calculations of the number of btc, benzo and missing linker based on the experimental MOF/residue ratio by assuming this model.

Sample	Missing Linker	ML%	Coordination positions
MUV-10	-0.073	-5.25	13.04
benzo25%-L	0.148	11.07	13.96
benzo50%-L	0.199	14.90	13.76
benzo70%-L	0.222	16.66	14.14
benzo80%-L	0.357	26.74	15.04

-Model structure: TiO_2@[$TiCaO(H_2O)_W(btc)_X(iso)_y(fa)_z(OH)_D$][13]

Table S35: Tabulated calculations of the number of btc, benzo and missing linker based on the experimental MOF/residue ratio by assuming this model. Note that the negative OH- values have been omitted when calculating the number of H_2O, otherwise it would be even higher.

Sample	R% TiO_2	btc	fa	benzo	OH	H_20	ML%	CP	S% TiO_2
MUV-10	0.072	1.511	0.015	0.000	-0.548	2.1	-13.36	13.66	0.023
benzo 25%-L	0.196	1.475	0.262	0.014	-0.717	3.8	-2.55	14.42	0.063
benzo 50%-L	0.192	1.404	0.310	0.018	-0.558	3.9	-5.15	14.57	0.063
benzo 70%-L	0.213	1.413	0.207	0.026	-0.497	4.8	-7.80	13.18	0.070
benzo 80%-L	0.342	1.485	0.355	0.046	-0.902	7.8	-6.33	14.08	0.110

S.8. Effect of modulation in the properties of MUV-10 H defective phases

S.8.1. Morphology and particle size of iso%-H series.

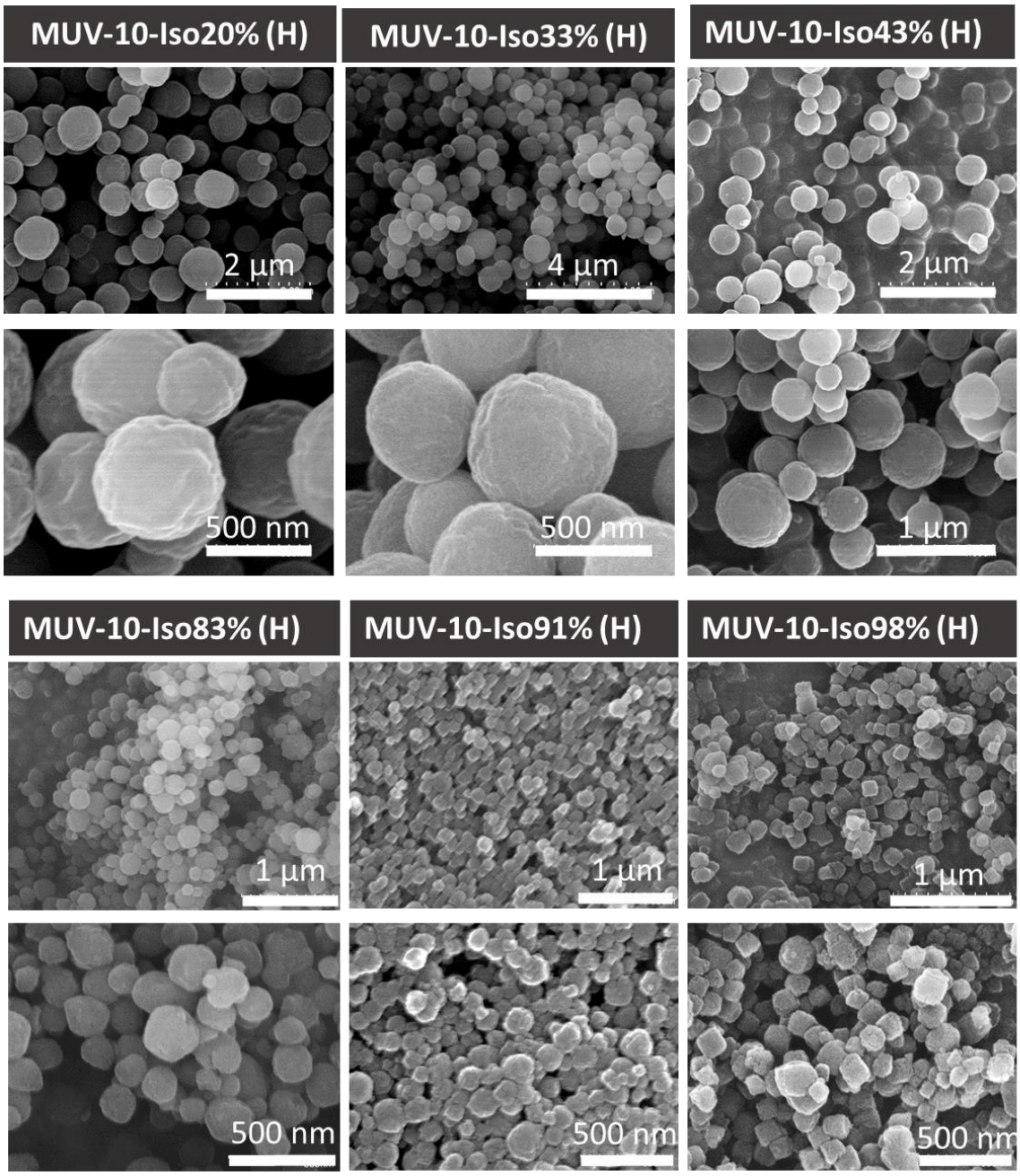

Figure S22: SEM images of iso%-H phases showing changes in morphology and particle size with increasing concentration of modulator.

Table S36: Tabulated particle sizes and standard deviations of iso%-H.

Sample	Particle size (µm)	Standard deviation (µm)
MUV-10 H	3.064	1.300
iso20%-H	0.641	0.171
iso33%-H	0.612	0.154
iso43%-H	0.532	0.096
iso83%-H	0.234	0.051
iso91%-H	0.114	0.024
iso98%-H	0.144	0.029

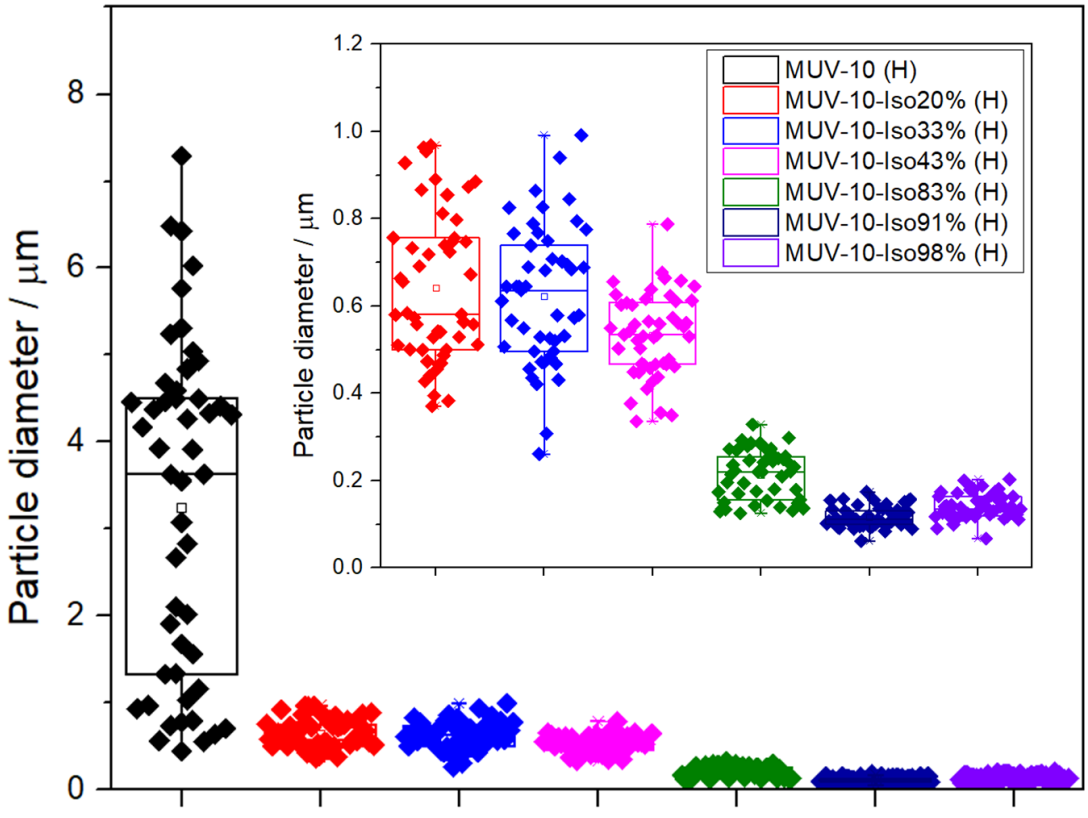

Figure S23: Box chart statistical representation of iso%-H particle sizes. Bin size of 50 nm, particle count of 50. Average size and standard deviation, 25% and 75% quartiles.

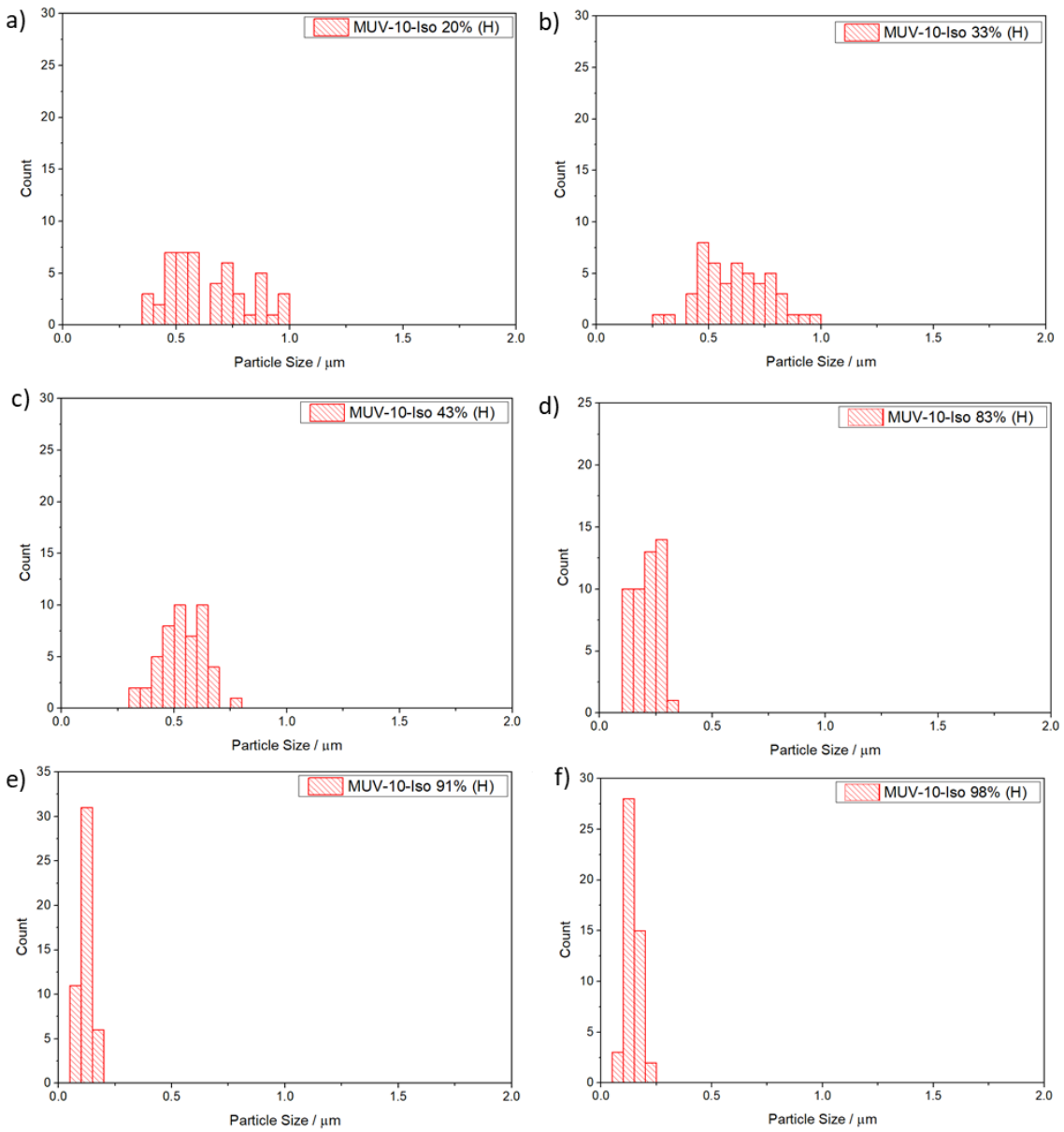

Figure S24: Individual particle size histograms of iso%-H. Bin size of 50 nm and particle count of 50.

S.8.1. Morphology and particle size of benzo%-H series.

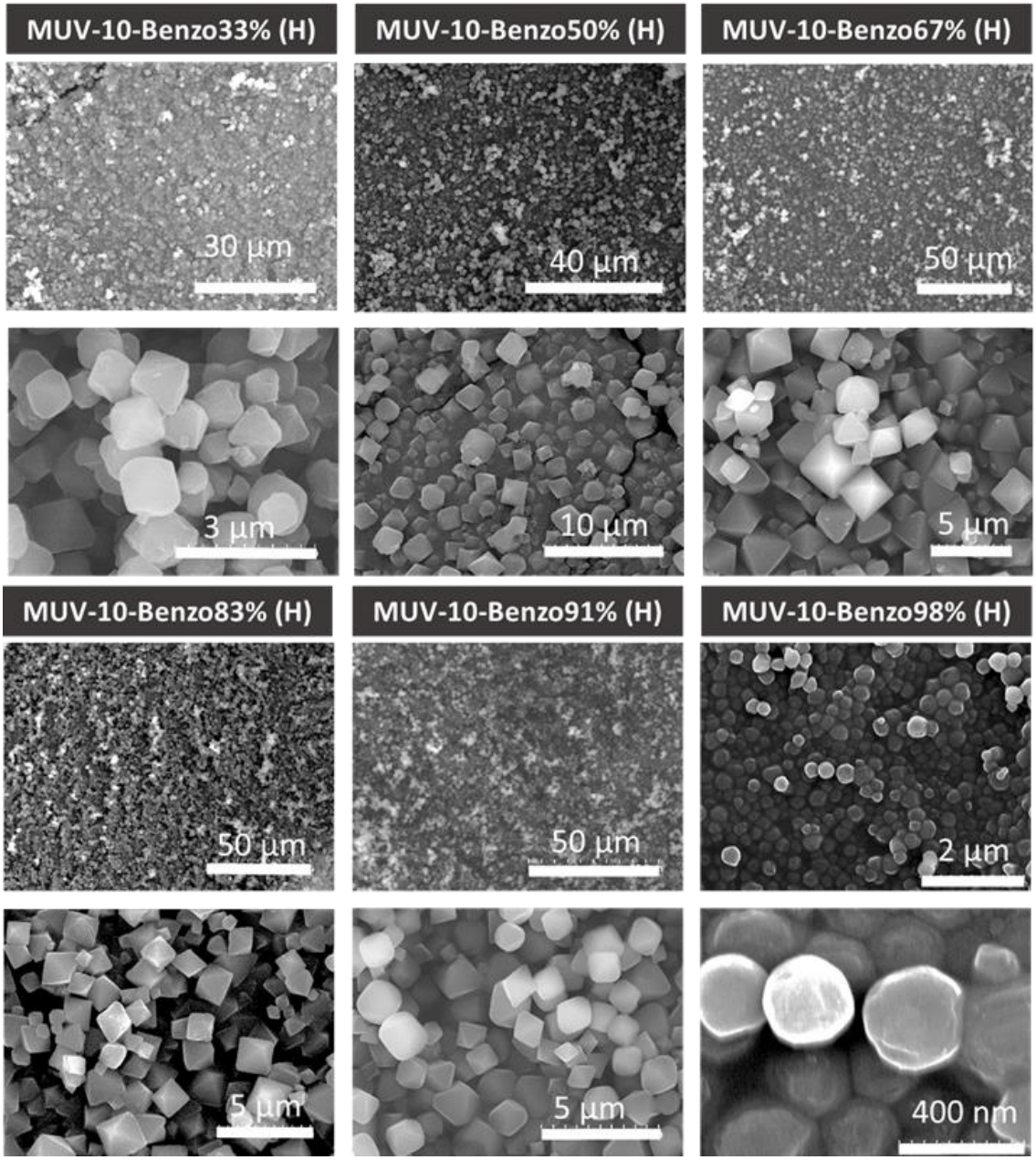

Figure S25: SEM images of benzo%-H, showing changes in morphology with more rounded corners compared to pristine MUV-10 possibly as a consequence of partial incorporation on the surface, with benzo98% H presenting a similar morphology to iso98% H.

Table S37: Tabulated particle sizes and standard deviations of benzo%-H.

Sample	Particle size (µm)	Standard deviation (µm)
MUV-10 H	3.064	1.300
benzo33%-H	1.357	0.237
benzo50%-H	2.820	0.356
benzo67%-H	3.690	0.358
benzo83%-H	2.329	0.316
benzo91%-H	2.475	0.445
benzo98%-H	0.288	0.039

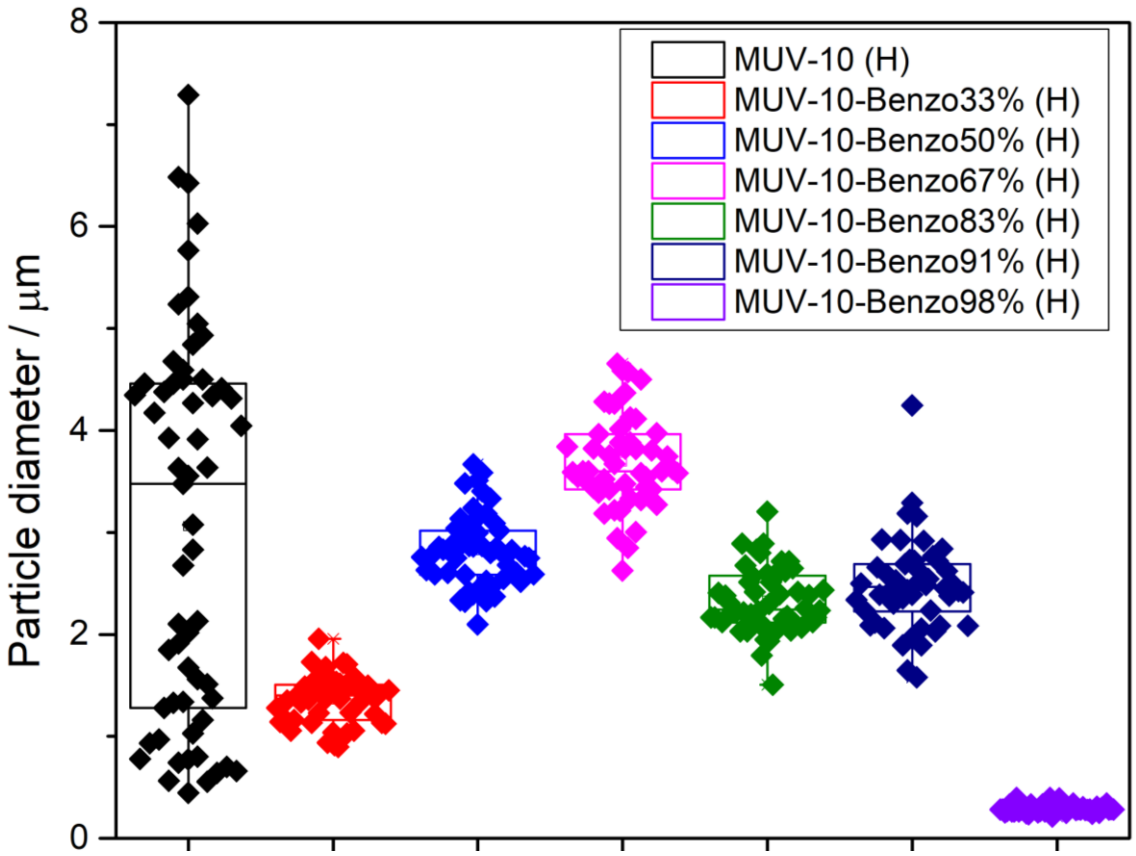

Figure S26: Box chart representation of benzo%-H particle sizes. Bin size of 50 nm. Bin size of 50 nm, particle count of 50. Average size and standard deviation, 25% and 75% quartiles.

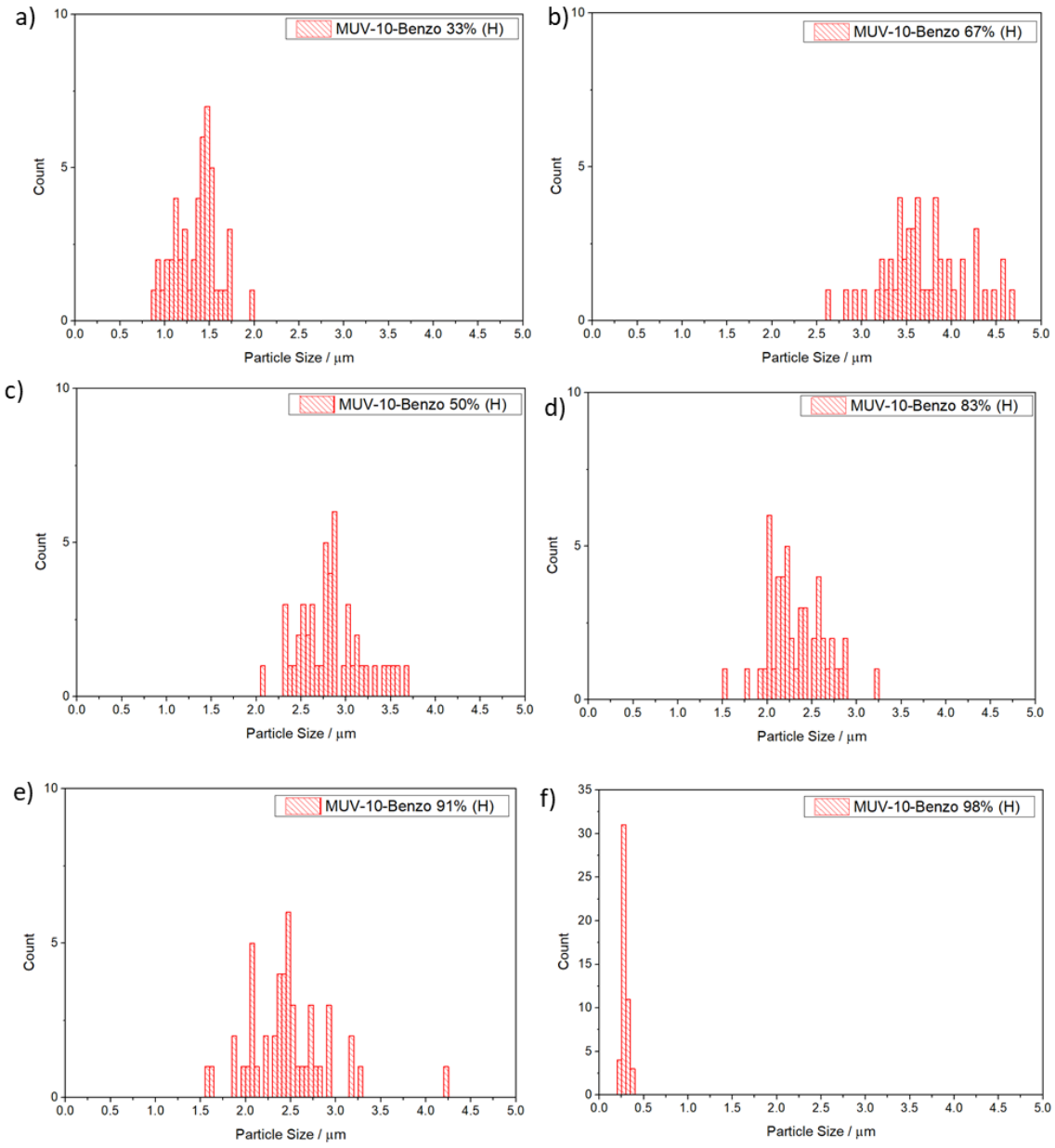

Figure S27: Individual particle size histograms of benzo%-H samples. Bin size of 50 nm. Bin size of 50 nm and particle count of 50.

S.8.2. Water stability of iso% and benzo%-H series for most defective samples.

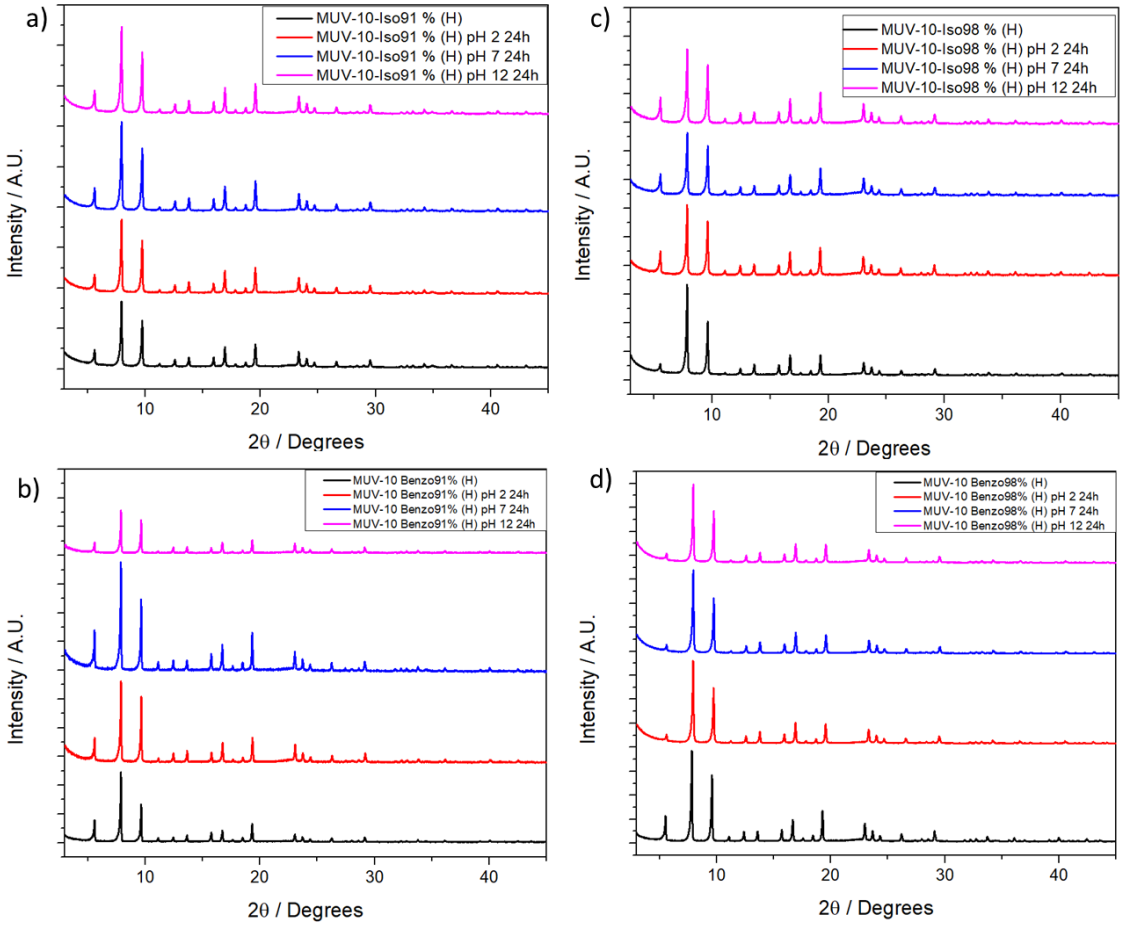

Figure S28: PXRD of the most defective iso H and benzo H samples after dispersion in water at different pH for 24 hours, showing stability.

S.8.3. Effect of defectivity in the dispersability of the samples in water and dichloromethane.

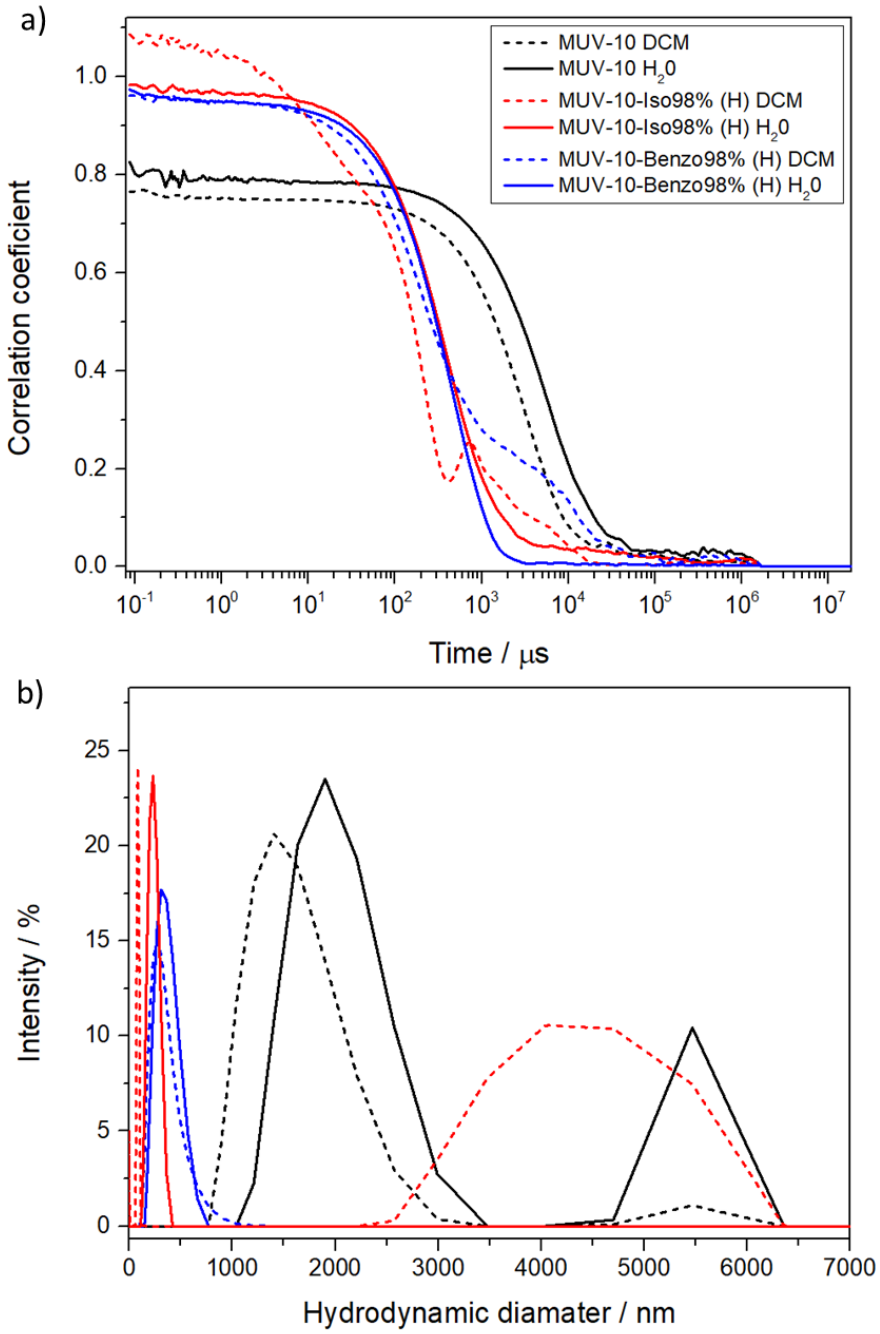

Figure S29: Comparison of a) correlograms of dispersions in water and DCM and b) hydrodynamic diameters obtained from the correlograms. The correlograms show that pristine MUV-10 disperses well in both DCM and water, indicating slightly higher particle sizes and sedimentation upon water dispersion. In contrast, both iso and benzo samples disperse well in water, while they do not in DCM. In fact, the correlograms in water indicate narrow size distribution of small size, while in DMC the appearance of aggregates is evident, some of which due to their high size are not present in the hydrodynamic diameter distribution of benzo98%-H. This indicates that defectivity increases the hydrophilicity of the samples.

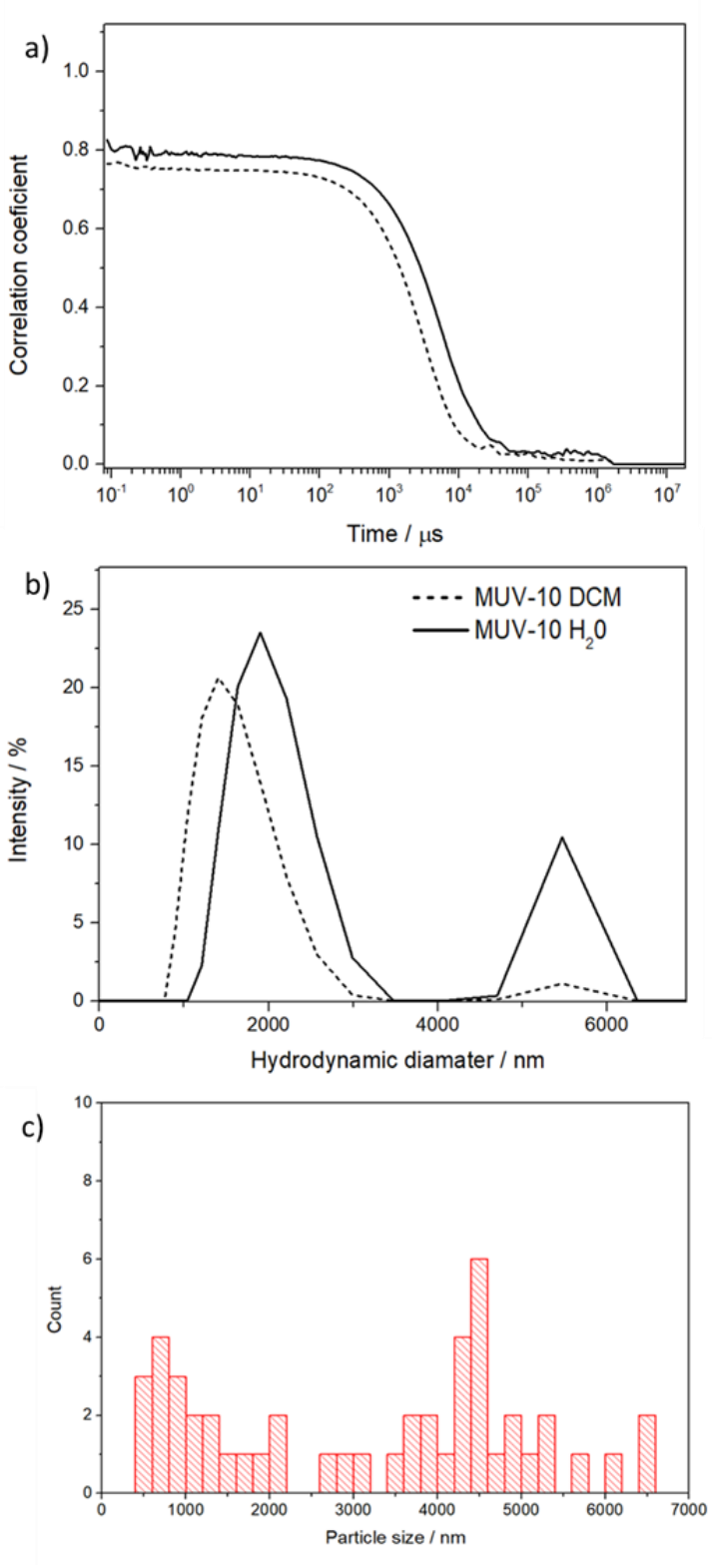

Figure S30: a) correlograms of dispersions in water and DCM b) hydrodynamic diameters obtained from the correlograms of MUV-10 dispersions in water and DCM and c) particle size distributions determined by SEM. Pristine MUV-10 displays particle sizes like those determined by SEM, with slightly better dispersity in DCM than in water. Additionally, the correlograms indicate that there is sedimentation in the water dispersion. This indicates that pristine MUV-10 is slightly more hydrophobic than hydrophilic.

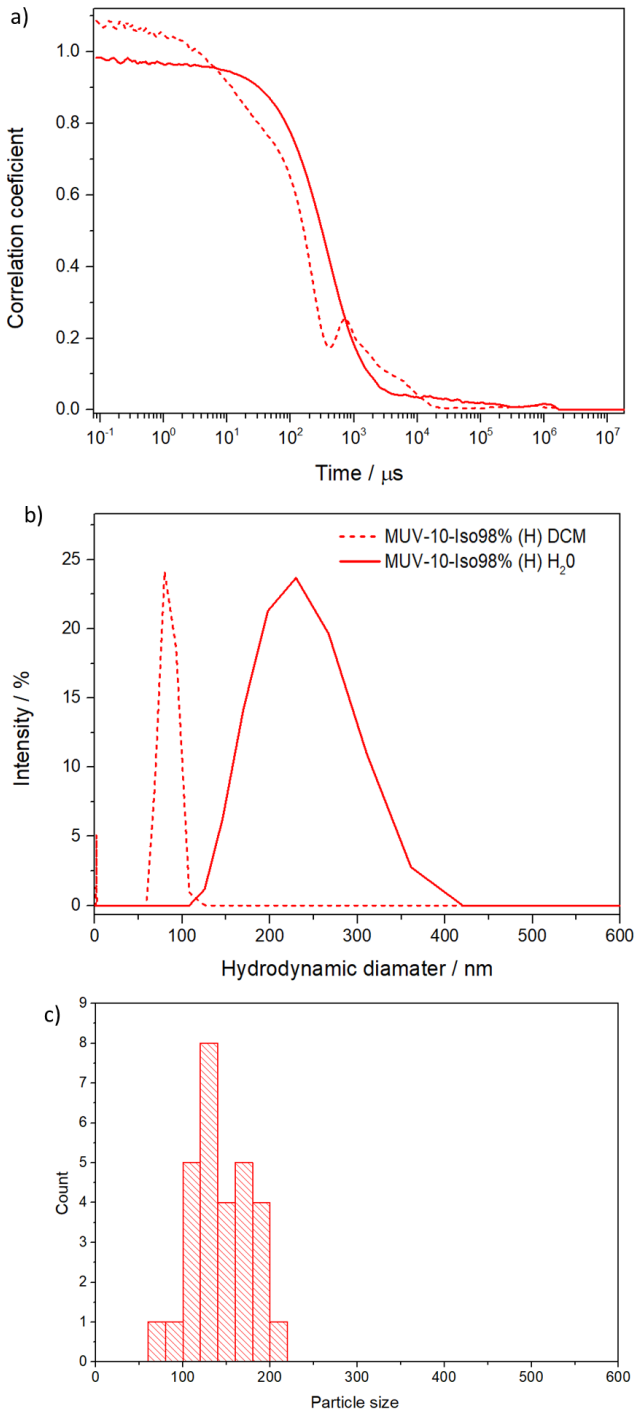

Figure S31: a) correlograms of dispersions in water and DCM, b) hydrodynamic diameters obtained from the correlograms of iso98%-H dispersions in water and DCM and c) particle size distributions determined by SEM. iso98%-H displays water hydrodynamic diameters similar to the particle sizes determined by SEM, with correlograms showing narrow distributions and no mayor aggregates or sediments. In contrast, DMC correlograms show the presence of different populations due to poor dispersion, with two populations, one smaller than in water and one being fundamentally aggregates that result in ca. 4.5 µm in size. This indicates that iso98% H is highly hydrophilic.

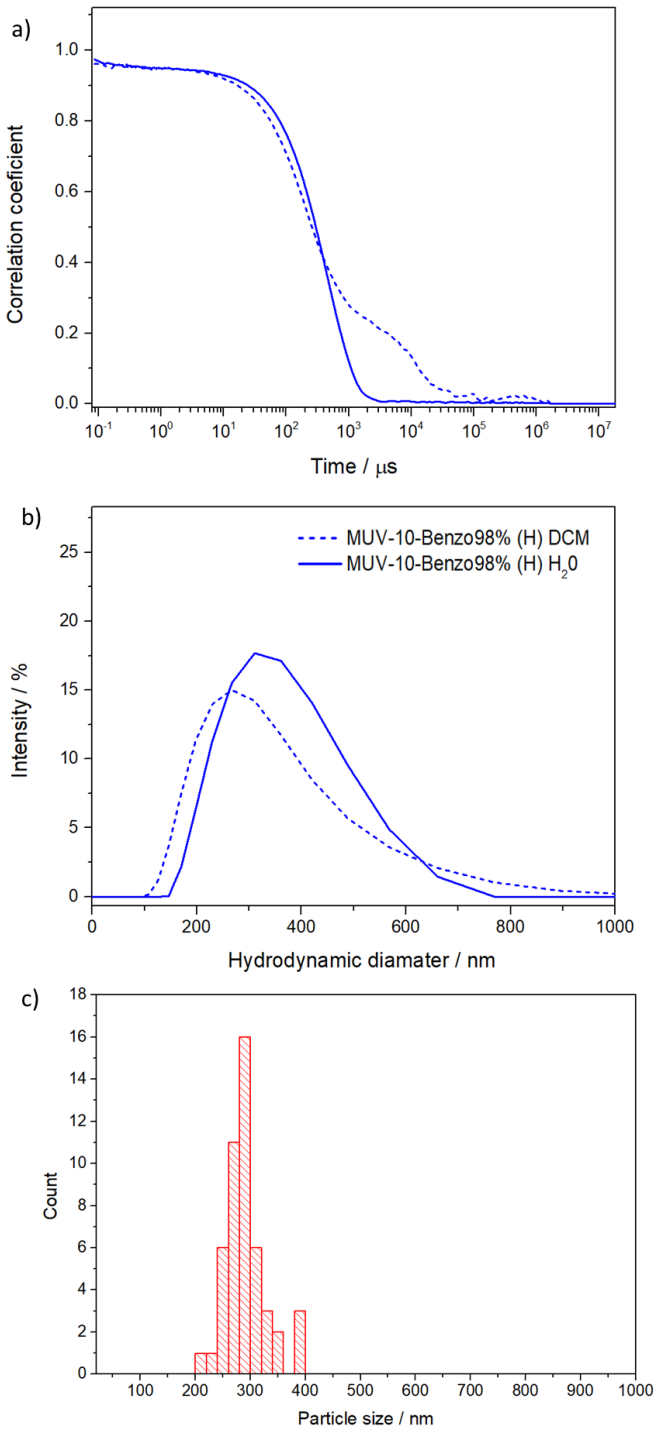

Figure S32: a) correlograms of dispersions in water and DCM, b) hydrodynamic diameters obtained from the correlograms of benzo98%-H dispersions in water and DCM and c) particle size distributions determined by SEM. benzo98%-H displays water hydrodynamic diameters similar to the particle sizes determined by SEM, with correlograms showing narrow distributions and no mayor aggregates or sediments. In contrast, DMC correlograms show the presence of bigger populations due to poor dispersion. benzo hydrodynamic diameter in DCM is similar to water, likely due to aggregates being too big to be displayed in the hydrodynamic diameter distributions determined by DLS, which is also envisioned in the correlograms, showing a bigger population for benzo than for iso. This indicates that iso98%-H is highly hydrophilic.

S.8.4. Analysis of the porosity of iso% and benzo%-H series

Table S38: Tabulated porosimetry extracted from N_2 adsorption and desorption measurements of iso%-H samples.

Sample	S_{BET} / S_{MICRO} (m^2/g)	Micro / Meso pores volume (cm^3/g)		Total Pore volume (cm^3/g)
MUV-10 H	1041 / 975	0.365	0.008	0.373
iso20%-H	952 / 834	0.322	0.136	0.474
iso33%-H	881 / 787	0.308	0.151	0.461
iso43%-H	903 / 807	0.317	0.174	0.493
iso83%-H	1216 / 979	0.389	0.203	0.592
iso91%-H	1247 / 993	0.414	0.202	0.616
iso98%-H	1041 / 839	0.333	0.279	0.612

Table S39: Tabulated porosimetry extracted from N_2 adsorption and desorption measurements of benzo%-H samples.

Sample	S_{BET} / S_{MICRO} (m^2/g)	Micro / Meso pores volume (cm^3/g)		Total Pore volume (cm^3/g)
MUV-10 H	1041 / 975	0.365	0.0190	0.373
benzo33%-H	993 / 870	0.335	0.037	0.373
benzo50%-H	923 / 775	0.297	0.128	0.425
benzo67%-H	1004/933	0.361	0.055	0.416
benzo83%-H	996 / 872	0.338	0.094	0.432
benzo91%-H	823/ 634	0.240	0.246	0.486
benzo98%-H	986 / 827	0.322	0.132	0.453

To simulate the PSD distribution of iso-H 33% (8% missing linkers) and 98% (44% missing linkers) we substituted 4 and 32 random btc ligands from a MUV-10 (2 x 2 x 2) cell by iso and formate ligands. This procedure was repeated until 12 symmetry independent defective structures were obtained. The pore size for each configuration was simulated by using Zeo++ (chan_radious=probe_ratious=0.8 and num_samples=2000).[6] Finally, individual PSD were averaged and compared to experimental PSD as represented in **Figure S28**.

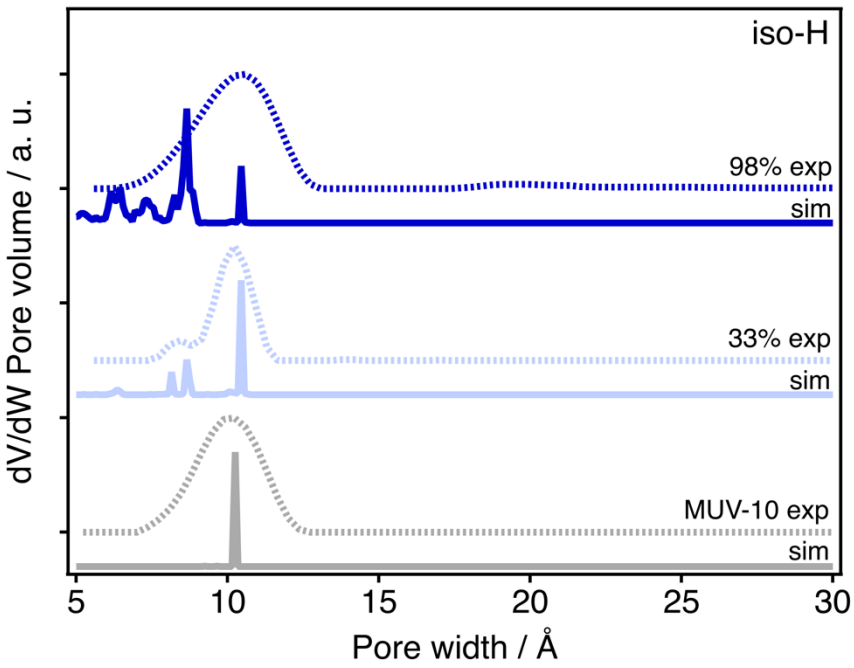

Figure S33: Experimental and simulated pore size distribution for iso-H 98%, 33% MUV-10. Simulated data have been shifted by -1.2 Å.

S.9. Effect of modulation in the properties of MUV-10 L defective phases

S.9.1. Morphology and particle size of iso and benzo%-L series.

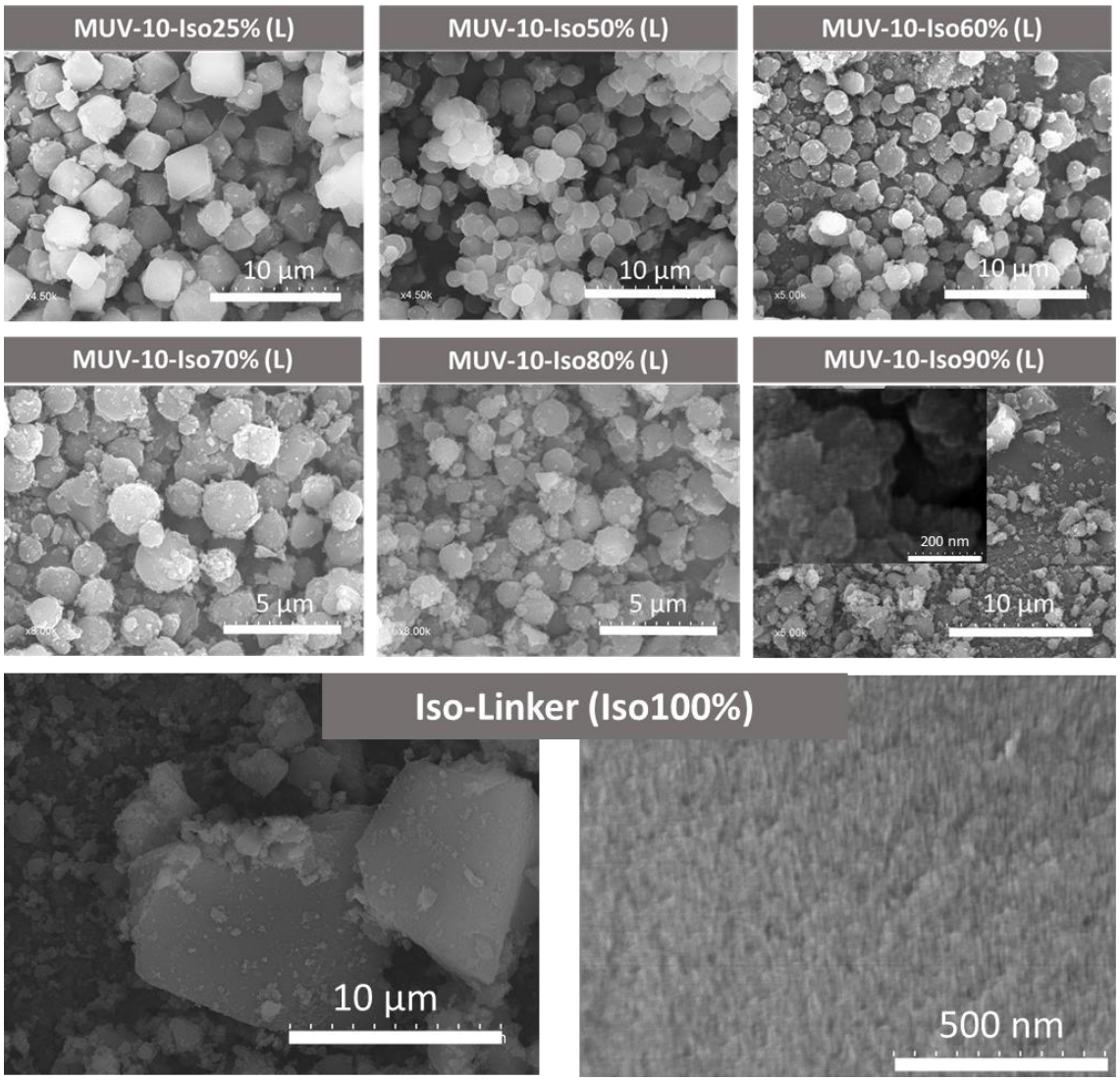

Figure S34: SEM images of iso%-L samples, showing a change in morphology compared to the pristine MOF, alongside with sample amorphization, possibly consequence of the formation of the iso 100% phase, which is composed of tiny nanoparticles.

Table S40: Tabulated particle sizes and standard deviations of iso%-L samples.

Sample	Particle size (µm)	Standard deviation (µm)
MUV-10 L	6.0	1.3
iso25%-L	3.153	0.565
iso50%-L	1.593	0.334
iso60%-L	1.388	0.311
iso70%-L	1.488	0.316
iso80%-L	1.413	0.314
iso90%-L	n/a	n/a

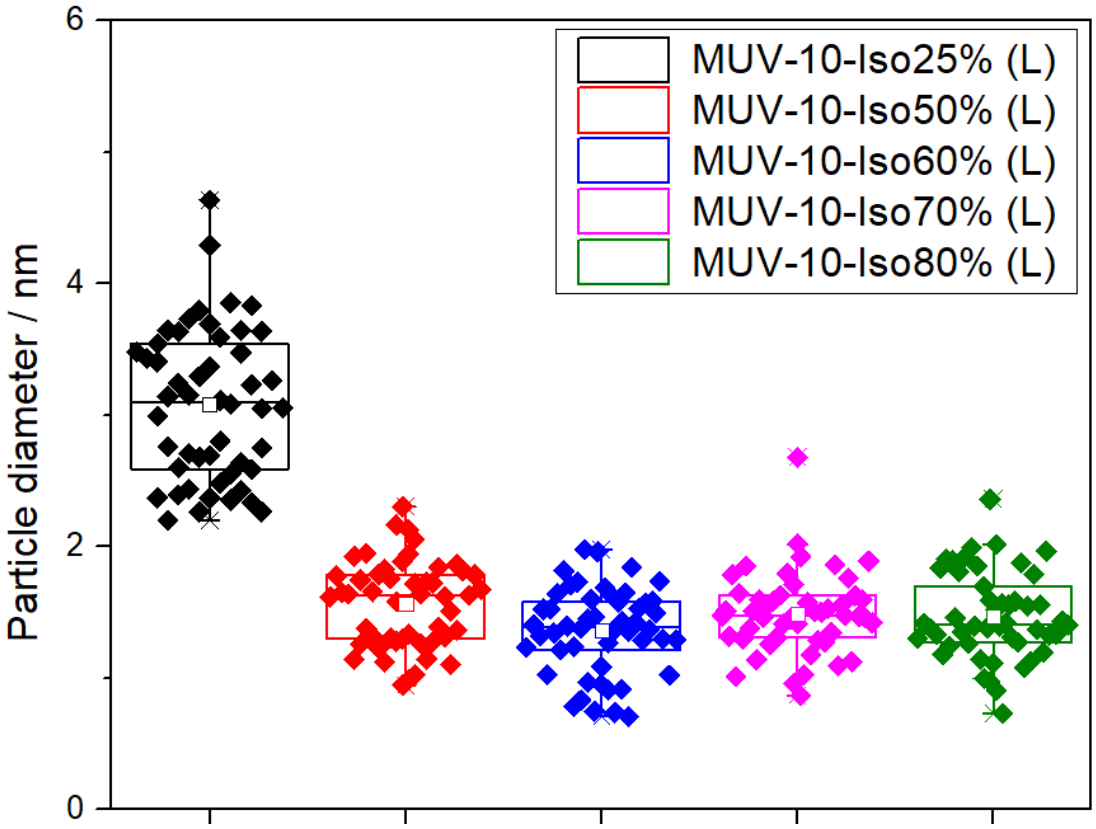

Figure S35: Box chart representation of iso%-L particle sizes. Bin size of 50 nm, particle count of 50. Average size and standard deviation, 25% and 75% quartiles.

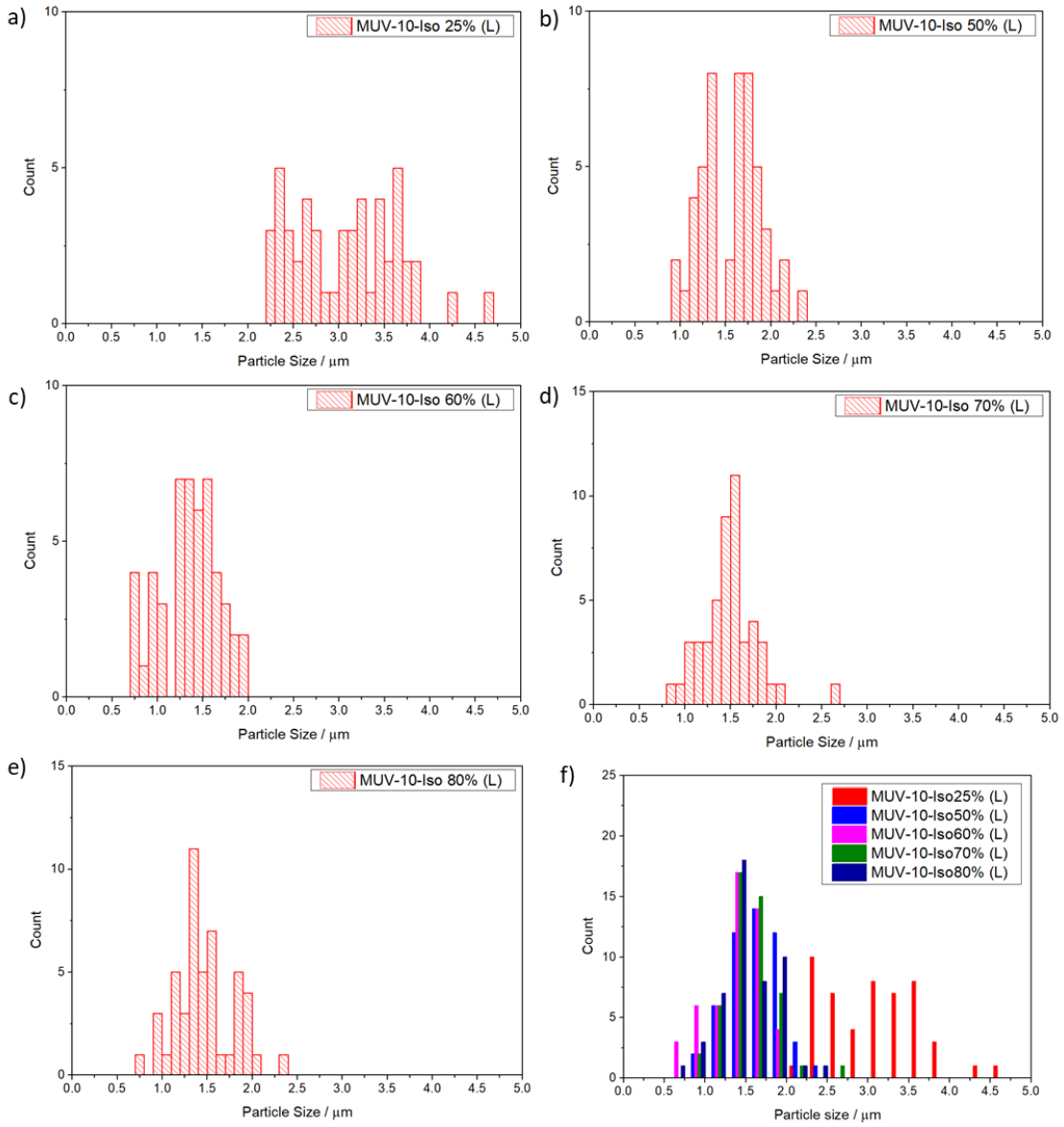

Figure S36: Particle size histograms of iso%-L. Bin size of 50 nm for individual profiles and 250 nm for comparison.

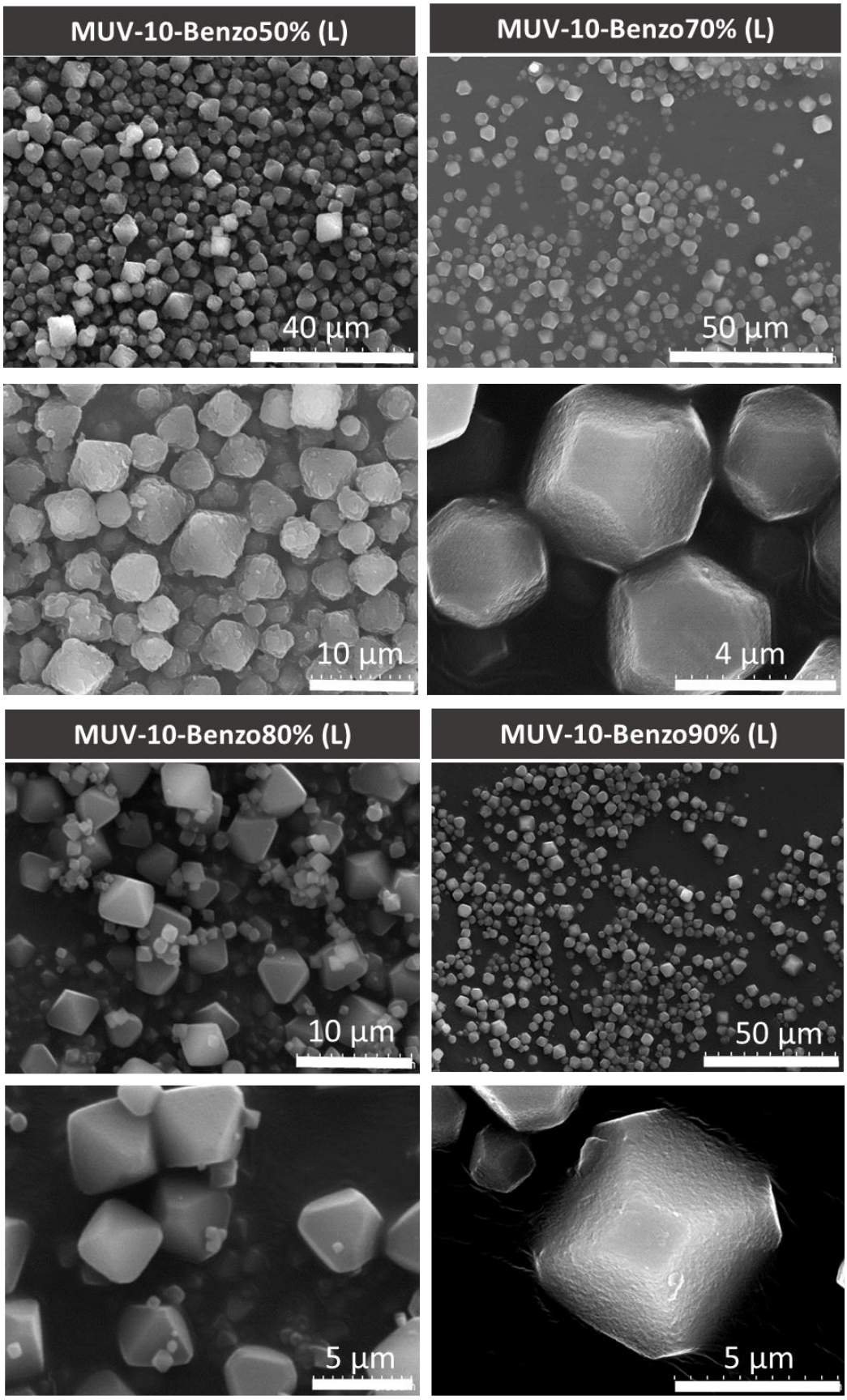

Figure S37: SEM images of benzo%-L modulated with benzoic acid, showing changes in morphology with more rounded corners compared to pristine MUV-10 possibly as a consequence of preferential surface incorporation.

Table S41: Tabulated Particle sizes and standard deviation of iso%-L samples

Sample	Particle size (µm)	Standard deviation (µm)
MUV-10 L	6.0	1.3
benzo50%-L	7.134	1.381
benzo70%-L	5.075	1.165
benzo80%-L	4.476	1.388
benzo90%-L	3.847	1.199

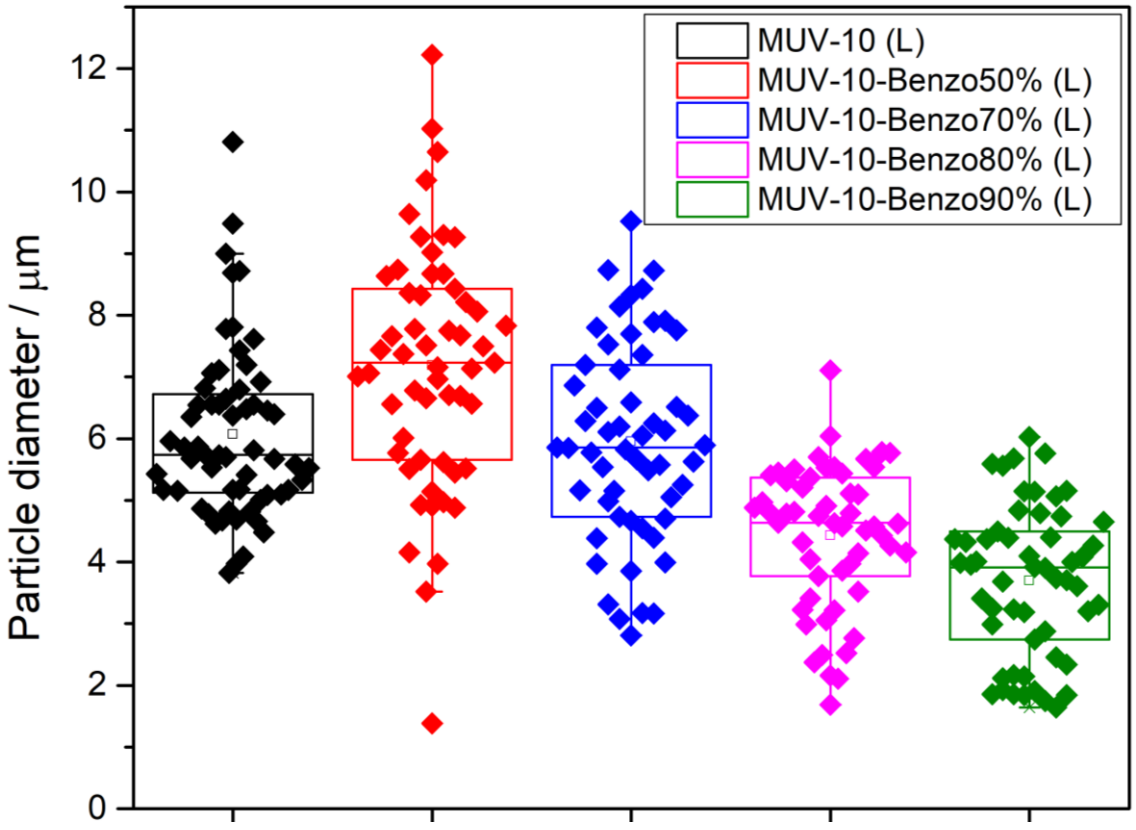

Figure S38: Box chart representation of benzo%-L particle sizes. Bin size of 200 nm, particle count of 50. Average size and standard deviation, 25% and 75% quartiles.

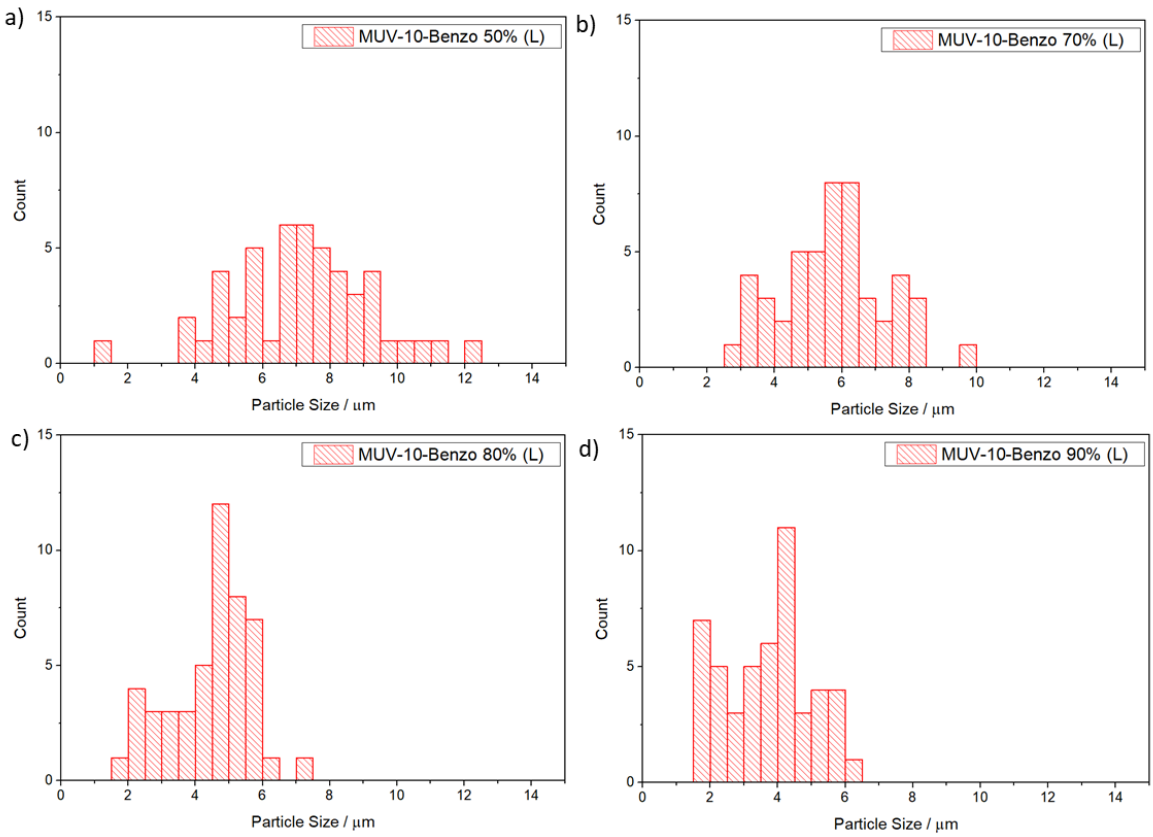

Figure S39: Particle size histograms of benzo%-L. Bin size of 500 nm.

S.9.2. Water stability of iso% and benzo%-L series

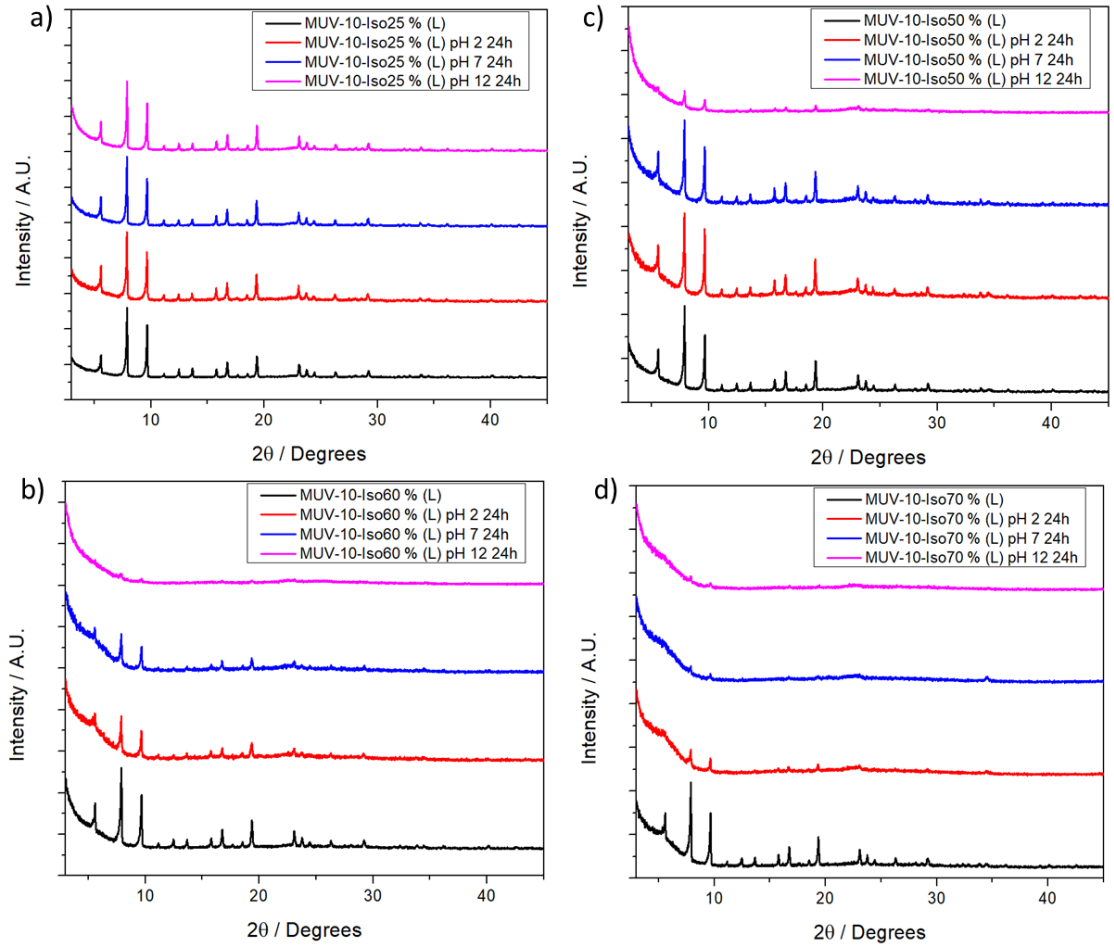

Figure S40: PXRD of iso%-L samples after dispersion in water at different pH for 24 hours.

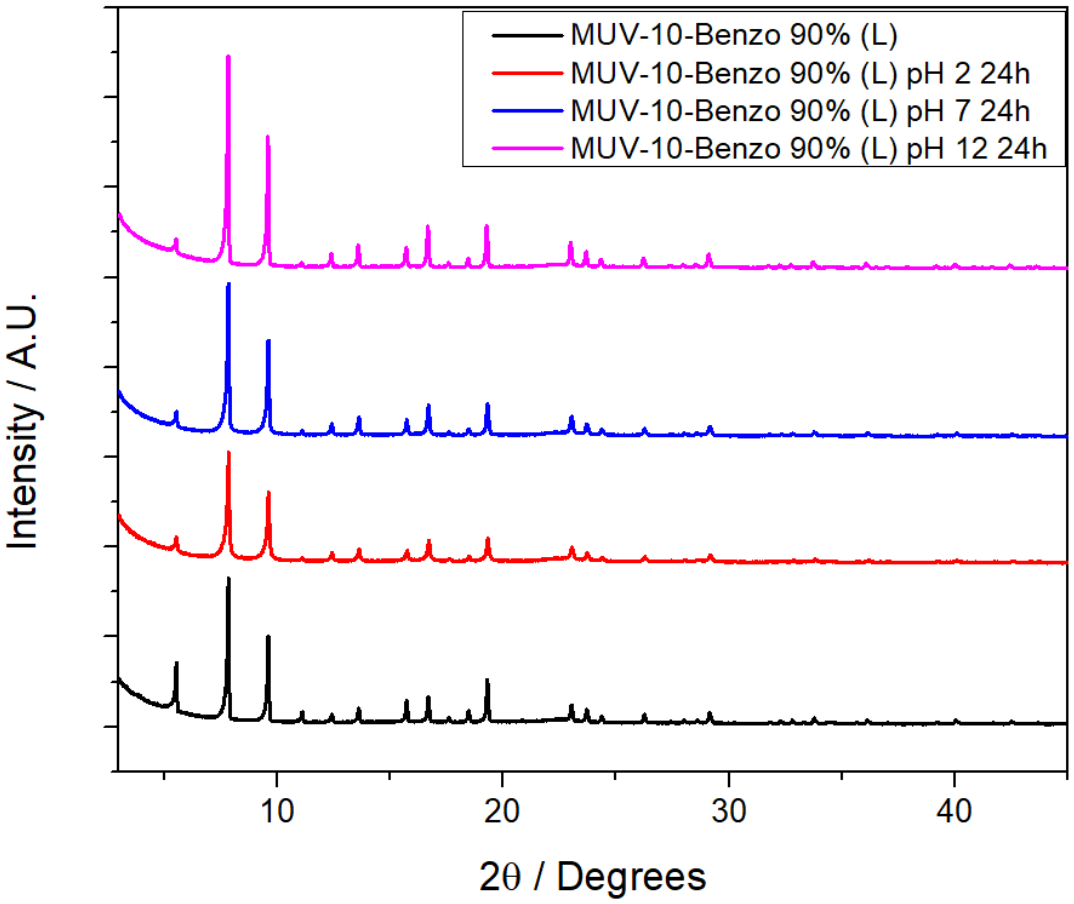

Figure S41: PXRD of the most defective benzo%-L sample after dispersion in water at different pH for 24 hours, showing stability.

S.9.3. Analysis of the porosity of iso% and benzo%-L series

Table S42: Tabulated porosimetry extracted from N_2 adsorption and desorption measurements of iso%-L samples, iso 100% phase and a physical mixture of MUV-10 and iso 100% phases.

Sample	S_{BET} / S_{MICRO} (m^2/g)	Micro/Meso pore volume (cm^3/g)		Total Pore volume (cm^3/g)
MUV-10 H	1041 / 975	0.365	0.00751	0.37251
iso25%-L	1064 / 846	0.328	0.103	0.431
iso50%-L	1114 / 792	0.312	0.142	0.454
iso60%-L	1038 / 640	0.256	0.207	0.463
iso70%-L	864 / 566	0.229	0.296	0.525
iso80%-L	916 / 347	0.141	0.460	0.601
iso90%-L	693 / na	Na	0.590	0.590
iso 100% phase	430/ na	Na	0.281	0.281
MUV-10, iso 100% (50% in weight)	562 / 360	0.17089	0.1731	0.344011

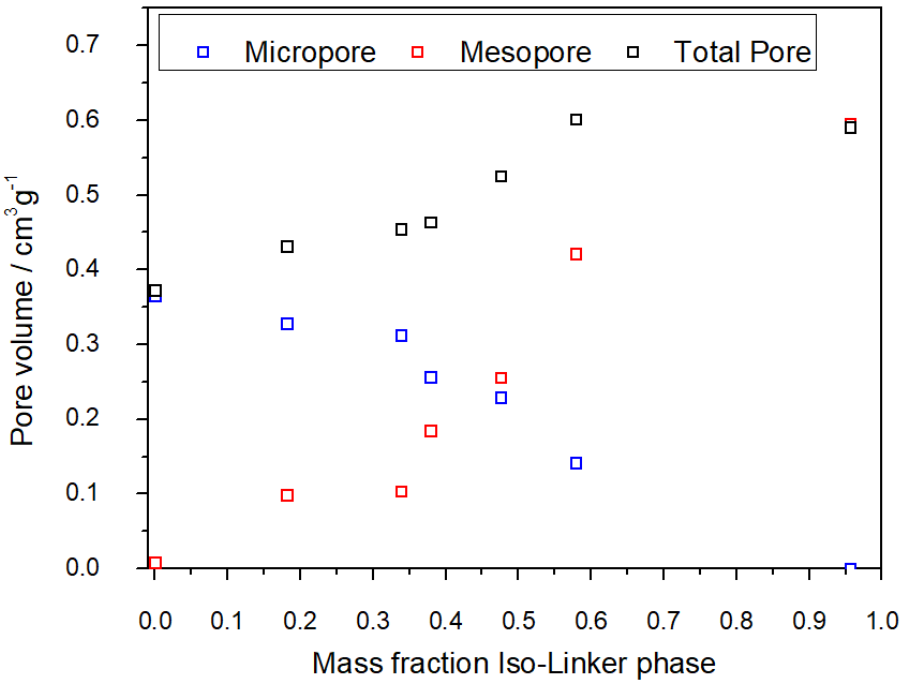

Figure S42: Changes in porosity metrics of iso%-L samples. The micropore, mesopore and total pore volumes are represented as a function of the mass fraction of iso 100% phase in comparison with MUV-10.

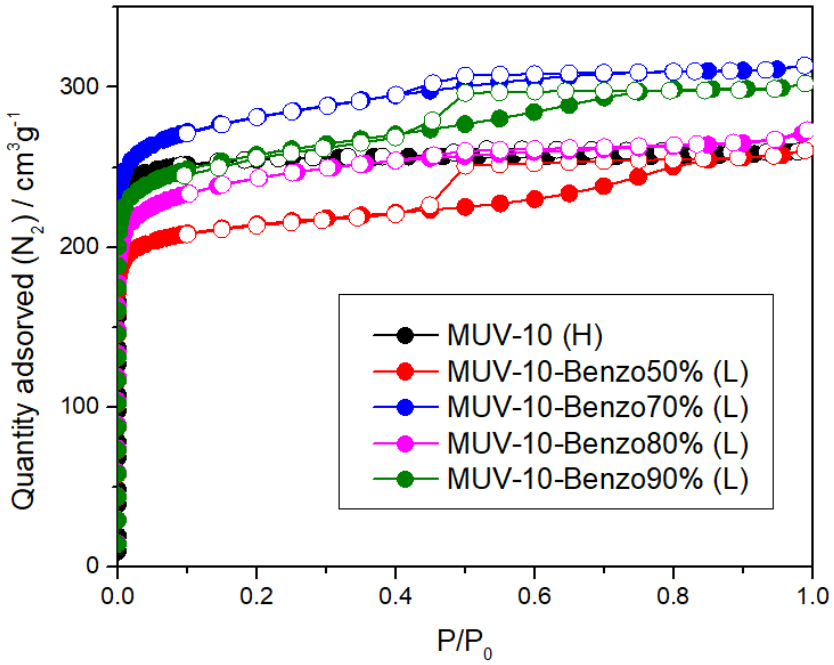

Figure S43: N_2 adsorption and desorption isotherms of benzo%-L series.

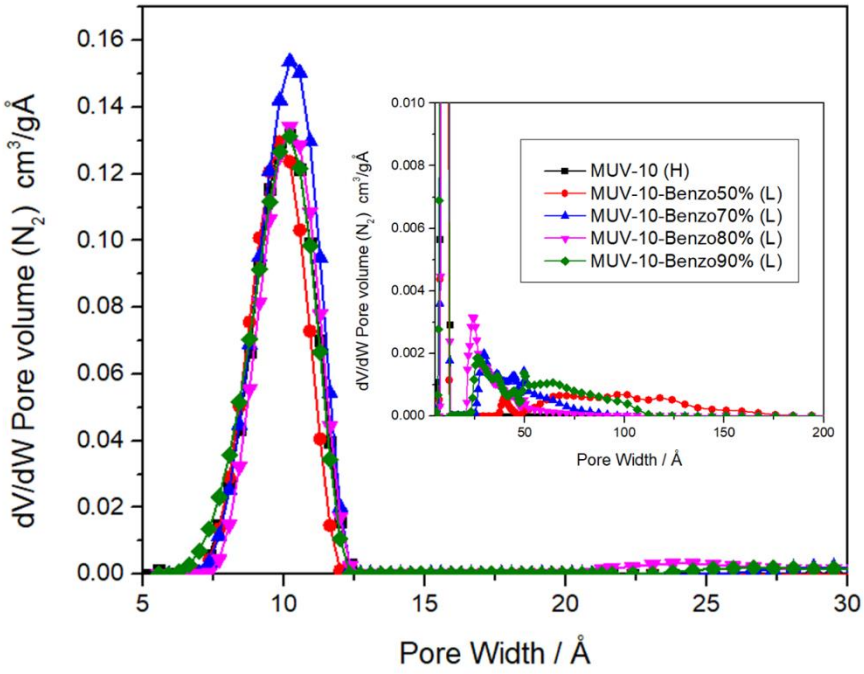

Figure S44: Pore size distributions of benzo%-L series by using the QSDT Cylindrical pore oxide surface model.

Table S43: Tabulated porosimetry extracted from N_2 adsorption and desorption measurements of benzo%-L samples.

Sample	**S_{BET} / S_{MICRO}** (m^2/g)	**Micro/Meso pore volume** (cm^3/g)		**Total Pore volume** (cm^3/g)
MUV-10 L	934/ 815	0.312	0.104	0.416
benzo50%-L	849 / 725	0.278	0.119	0.397
benzo70%-L	1081 / 873	0.345	0.136	0.482
benzo80%-L	923 /718	0.287	0.127	0.414
benzo90%-L	988 / 785	0.311	0.154	0.465

S.10 Comparison of thermal Stability

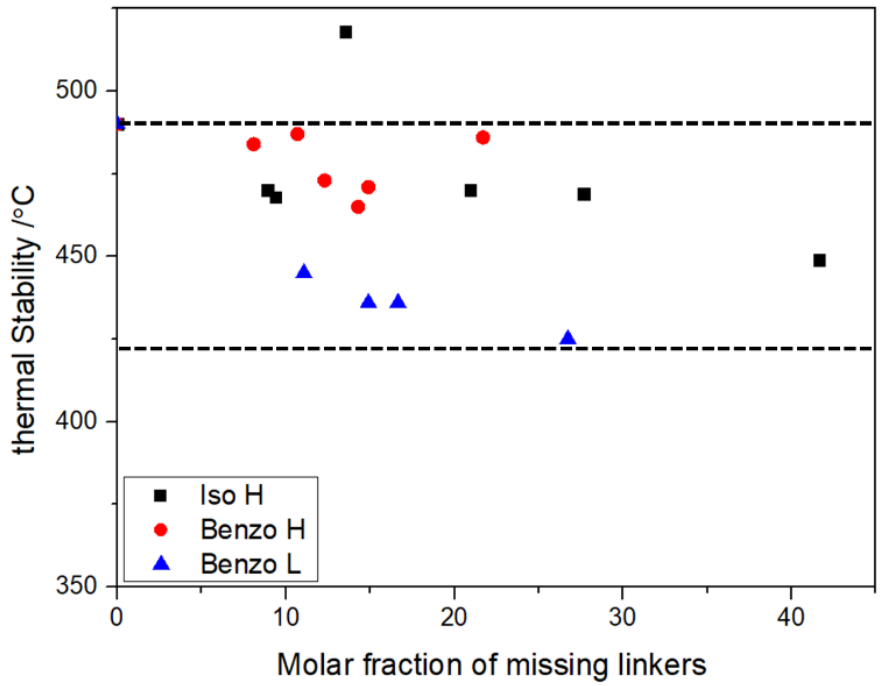

Figure S45: Comparison of the thermal decomposition temperature of the frameworks as a function of the molar per cent of missing linkers.

S.11 Electronic structure

We now want to investigate the effect of the missing linker in on the electronic structure of the MUV-10. We calculated the electronic density of states (DOS) and band alignment relative to the vacuum level for pristine MUV-10 and a single missing linker defect. The normalized total DOS of pristine MUV-10 and its defect structures with incorporation of different modulators: iso and benzo are shown in **Figure S46**. Our calculation shows that the band gap variation between pristine MUV-10 and the defective structures is 0.4 eV. The electronic properties of the material vary slightly in the direction unfavorable for photocalysis. Our calculation suggested that the impact in photocatalytic activity induced by missing linker defects will be minimal.

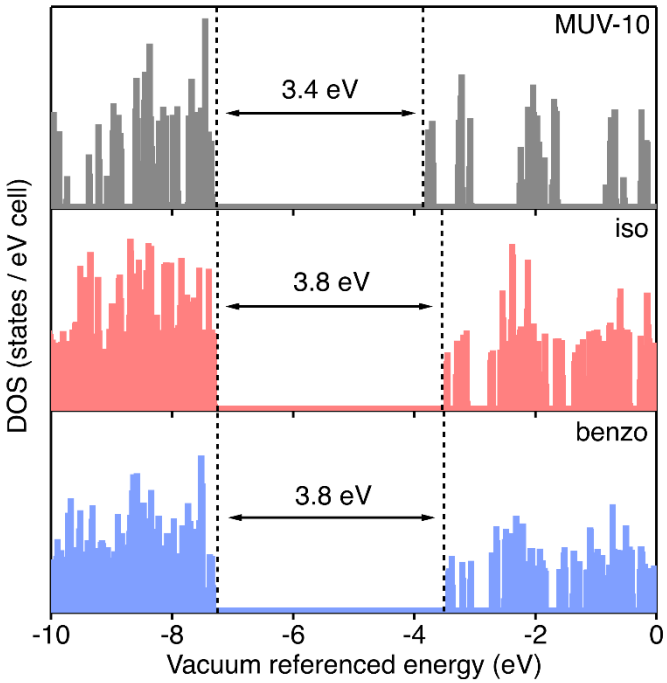

Figure S46. Electronic Total DOS spectra aligned relative to the vacuum level of pristine MUV-10 (top) and its defect structures with the incorporation of different modulators: iso (red) and benzo (blue).

S.11 References

1 J. P. Perdew, K. Burke and M. Ernzerhof, *Phys Rev Lett*, 1996, **77**, 3865–3868.

2 G. Kresse and J. Furthmüller, *Comp Mater Sci*, 1996, **6**, 15–50.

3 G. Kresse and J. Furthmüller, *Phys Rev B*, 1996, **54**, 11169–11186.

4 K. Lejaeghere, G. Bihlmayer, T. Björkman, P. Blaha, S. Blügel, V. Blum, D. Caliste, I. E. Castelli, S. J. Clark, A. D. Corso, S. de Gironcoli, T. Deutsch, J. K. Dewhurst, I. D. Marco, C. Draxl, M. Dułak, O. Eriksson, J. A. Flores-Livas, K. F. Garrity, L. Genovese, P. Giannozzi, M. Giantomassi, S. Goedecker, X. Gonze, O. Grånäs, E. K. U. Gross, A. Gulans, F. Gygi, D. R. Hamann, P. J. Hasnip, N. A. W. Holzwarth, D. Iuşan, D. B. Jochym, F. Jollet, D. Jones, G. Kresse, K. Koepernik, E. Küçükbenli, Y. O. Kvashnin, I. L. M. Locht, S. Lubeck, M. Marsman, N. Marzari, U. Nitzsche, L. Nordström, T. Ozaki, L. Paulatto, C. J. Pickard, W. Poelmans, M. I. J. Probert, K. Refson, M. Richter, G.-M. Rignanese, S. Saha, M. Scheffler, M. Schlipf, K. Schwarz, S. Sharma, F. Tavazza, P. Thunström, A. Tkatchenko, M. Torrent, D. Vanderbilt, M. J. van Setten, V. V. Speybroeck, J. M. Wills, J. R. Yates, G.-X. Zhang and S. Cottenier, *Science*, 2016, **351**, aad3000.

5 T. Bučko, S. Lebègue, J. Hafner and J. G. Ángyán, *Phys Rev B*, 2013, **87**, 064110.

6 J. Heyd, G. E. Scuseria and M. Ernzerhof, *J Chem Phys*, 2003, **118**, 8207–8215.

7 K. T. Butler, C. H. Hendon and A. Walsh, *J Am Chem Soc*, 2014, **136**, 2703–2706.

8 R. L. Martin, B. Smit and M. Haranczyk, *J Chem Inf Model*, 2011, **52**, 308–318.

9 J. Castells-Gil, N. M. Padial, N. Almora-Barrios, J. Albero, A. R. Ruiz-Salvador, J. González-Platas, H. García and C. Martí-Gastaldo, *Angewandte Chemie Int Ed*, 2018, **57**, 8453–8457.

10 N. M. Padial, B. Lerma-Berlanga, N. Almora-Barrios, J. Castells-Gil, I. da Silva, M. de la Mata, S. I. Molina, J. Hernández-Saz, A. E. Platero-Prats, S. Tatay and C. Marti-Gastaldo, *J Am Chem Soc*, , DOI:10.1021/jacs.0c00117.

11 G. C. Shearer, S. Chavan, S. Bordiga, S. Svelle, U. Olsbye and K. P. Lillerud, *Chemistry of Materials*, 2016, **28**, 3749 3761.

12 G. C. Shearer, S. Forselv, S. Chavan, S. Bordiga, K. Mathisen, M. Bjørgen, S. Svelle and K. P. Lillerud, *Top Catal*, 2013, **56**, 770–782.

13 I. A. Lázaro, *Eur J Inorg Chem*, , DOI:10.1002/ejic.202000656.